Spectroscopy and Such (Working Title)

By
Blaise Jonathan Thompson

A dissertation submitted in partial fulfillment of
the requirements for the degree of

Doctor of Philosophy
(Chemistry)

at the
UNIVERSITY OF WISCONSIN - MADISON
20xx

Date of final oral examination: xx/xx/xxxx
This dissertation is approved by the following members of the Final Oral Committee:
John C. Wright, Professor, Analytical Chemistry
x
x
x
x

Contents

List of Figures

List of Tables

Acknowledgments

Abstract

The explanatory stories that people find compelling are simple; are concrete rather than abstract; assign a larger role to talent, stupidity and intentions than to luck; and focus on a few striking events that happened rather than on the countless events that failed to happen.

The ultimate test of an explanation is whether it would have made the event predictable in advance.

Paradoxically, it is easier to construct a coherent story when you know little, when there are fewer pieces to fit into the puzzle. Our comforting conviction that the world makes sense rests on a secure foundation: our almost unlimited ability to ignore our ignorance.

– Daniel Kahneman [1]

Part I

Background

Chapter 1

Introduction

1.1 Coherent Multidimensional Spectroscopy

CMDS, coherent multidimensional spectroscopy

1.2 The CMDS Instrument

1.3 Scientific Software

Chapter 2

Spectroscopy

In this chapter I lay out the foundations of spectroscopy.

2.1 Light

2.2 Light-Matter Interaction

Spectroscopic experiments all derive from the interaction of light and matter. Many material properties can be deduced by measuring the nature of this interaction.

Nonlinear spectroscopy relies upon higher-order terms in the light-matter interaction. In a generic system, each term is roughly ten times smaller than the last.

2.2.1 Representations

Many strategies have been introduced for diagrammatically representing the interaction of multiple electric fields in an experiment.

Circle Diagrams

Double-sided Feynman Diagrams

WMEL Diagrams

So-called wave mixing energy level (WMEL) diagrams are the most familiar way of representing spectroscopy for Wright group members. WMEL diagrams were first proposed by Lee and Albrecht in an appendix to their seminal work *A Unified View of Raman, Resonance Raman, and Fluorescence Spectroscopy* [2]. WMEL diagrams are drawn using the following rules.

1. The energy ladder is represented with horizontal lines - solid for real states and dashed for virtual states.
2. Individual electric field interactions are represented as vertical arrows. The arrows span the distance between the initial and final state in the energy ladder.
3. The time ordering of the interactions is represented by the ordering of arrows, from left to right.
4. Ket-side interactions are represented with solid arrows.
5. Bra-side interactions are represented with dashed arrows.
6. Output is represented as a solid wavy line.

Mukamel Diagrams

2.3 Linear Spectroscopy

2.3.1 Reflectivity

This derivation adapted from *Optical Processes in Semiconductors* by Jacques I. Pankove [3]. For normal incidence, the reflection coefficient is

$$R = \frac{(n-1)^2 + k^2}{(n+1)^2 + k^2} \tag{2.1}$$

Further derivation adapted from [4]. To extend reflectivity to a differential measurement

2.4 Coherent Multidimensional Spectroscopy

multiresonant coherent multidimensional spectroscopy

2.4.1 Three Wave

2.4.2 Four Wave

Fluorescence

Raman

2.4.3 Five Wave

2.4.4 Six Wave

multiple population-period transient spectroscopy (MUPPETS)

2.5 Strategies for CMDS

2.5.1 Homodyne vs. Heterodyne Detection

Two kinds of spectroscopies: 1) heterodyne 2) homodyne. Heterodyne techniques may be self heterodyne or explicitly heterodyned with a local oscillator.

In all heterodyne spectroscopies, signal goes as N. In all homodyne spectroscopies, signal goes as N^2. This literally means that homodyne signals go as the square of heterodyne signals, which is what we mean when we say that homodyne signals are intensity level and heterodyne signals are amplitude level.

Transient absorption, TA

2.5.2 Frequency vs. Time Domain

Time domain techniques become more and more difficult when large frequency bandwidths are needed. With very short, broad pulses:

- Non-resonant signal becomes brighter relative to resonant signal
- Pulse distortions become important.

This epi-CARS paper might have some useful discussion of non-resonant vs resonant for shorter and shorter pulses [5].

An excellent discussion of pulse distortion phenomena in broadband time-domain experiments was published by Spencer et al. [6].

Another idea in defense of frequency domain is for the case of power studies. Since time-domain pulses in-fact possess all colors in them they cannot be trusted as much at perturbative fluence. See that paper that Natalia presented...

2.5.3 Triply Electronically Enhanced Spectroscopy

Triply Electronically Enhanced (TrEE) spectroscopy has become the workhorse homodyne-detected 4WM experiment in the Wright Group.

2.5.4 Transient Absorbance Spectroscopy

Transient absorption (TA)

Quantitative TA

Transient absorbance (TA) spectroscopy is a self-heterodyned technique. Through chopping you can measure nonlinearities quantitatively much easier than with homodyne detected (or explicitly heterodyned) experiments.

Figure 2.1 diagrams the TA measurement for a generic sample. Here I show measurement of both the reflected and transmitted probe beam . . . not important in opaque (pyrite) or non-reflective (quantum dot) samples . . .

Typically one attempts to calculate the change in absorbance ΔA . . .

$$\begin{aligned}
\Delta A &= A_{\text{on}} - A_{\text{off}} && (2.2)\\
&= -\log_{10}\left(\frac{I_{\text{T}} + I_{\text{R}} + I_{\Delta\text{T}} + I_{\Delta\text{R}}}{I_0}\right) + \log\left(\frac{I_{\text{T}} + I_{\text{R}}}{I_0}\right) && (2.3)\\
&= -\left(\log_{10}(I_{\text{T}} + I_{\text{R}} + I_{\Delta\text{T}} + I_{\Delta\text{R}}) - \log_{10}(I_0)\right) + \left(\log_{10}(I_{\text{T}} + I_{\text{R}}) - \log_{10}(I_0)\right) && (2.4)\\
&= -\left(\log_{10}(I_{\text{T}} + I_{\text{R}} + I_{\Delta\text{T}} + I_{\Delta\text{R}}) - \log_{10}(I_{\text{T}} + I_{\text{R}})\right) && (2.5)\\
&= -\log_{10}\left(\frac{I_{\text{T}} + I_{\text{R}} + I_{\Delta\text{T}} + I_{\Delta\text{R}}}{I_{\text{T}} + I_{\text{R}}}\right) && (2.6)
\end{aligned}$$

Equation 2.6 simplifies beautifully if reflectivity is negligible ...

Now I define a variable for each experimental measurable:

V_{T}	voltage recorded from transmitted beam, without pump
V_{R}	voltage recorded from reflected beam, without pump
$V_{\Delta\text{T}}$	change in voltage recorded from transmitted beam due to pump
$V_{\Delta\text{R}}$	change in voltage recorded from reflected beam due to pump

We will need to calibrate using a sample with a known transmisivity and reflectivity constant:

$V_{\text{T, ref}}$	voltage recorded from transmitted beam, without pump
$V_{\text{R, ref}}$	voltage recorded from reflected beam, without pump
$\mathcal{T}_{\text{ref}}$	transmissivity
$\mathcal{R}_{\text{ref}}$	reflectivity

Define two new proportionality constants...

$$\begin{aligned}
C_{\text{T}} &\equiv \frac{\mathcal{T}}{V_{\text{T}}} && (2.7)\\
C_{\text{R}} &\equiv \frac{\mathcal{R}}{V_{\text{R}}} && (2.8)
\end{aligned}$$

These are explicitly calibrated (as a function of probe color) prior to the experiment using the calibration sample.

Given the eight experimental measurables (V_{T}, V_{R}, $V_{\Delta\text{T}}$, $V_{\Delta\text{R}}$, $V_{\text{T, ref}}$, $V_{\text{R, ref}}$, $\mathcal{T}_{\text{ref}}$, $\mathcal{R}_{\text{ref}}$) I can express all of the intensities in Equation 2.6 in terms of I_0.

$$
\begin{aligned}
C_\mathrm{T} &= \frac{\mathcal{T}_\mathrm{ref}}{V_\mathrm{T,\,ref}} && (2.9)\\
C_\mathrm{R} &= \frac{\mathcal{R}_\mathrm{ref}}{V_\mathrm{R,\,ref}} && (2.10)\\
I_\mathrm{T} &= I_0 C_\mathrm{T} V_\mathrm{T} && (2.11)\\
I_\mathrm{R} &= I_0 C_\mathrm{R} V_\mathrm{R} && (2.12)\\
I_{\Delta\mathrm{T}} &= I_0 C_\mathrm{T} V_{\Delta\mathrm{T}} && (2.13)\\
I_{\Delta\mathrm{R}} &= I_0 C_\mathrm{R} V_{\Delta\mathrm{R}} && (2.14)
\end{aligned}
$$

Wonderfully, the I_0 cancels when plugged back in to Equation 2.6, leaving a final expression for ΔA that only depends on my eight measurables.

$$\Delta A = -\log_{10}\left(\frac{C_\mathrm{T}(V_\mathrm{T} + V_{\Delta\mathrm{T}}) + C_\mathrm{R}(V_\mathrm{R} + V_{\Delta\mathrm{R}})}{C_\mathrm{T} V_\mathrm{T} + C_\mathrm{R} V_\mathrm{R}}\right) \tag{2.15}$$

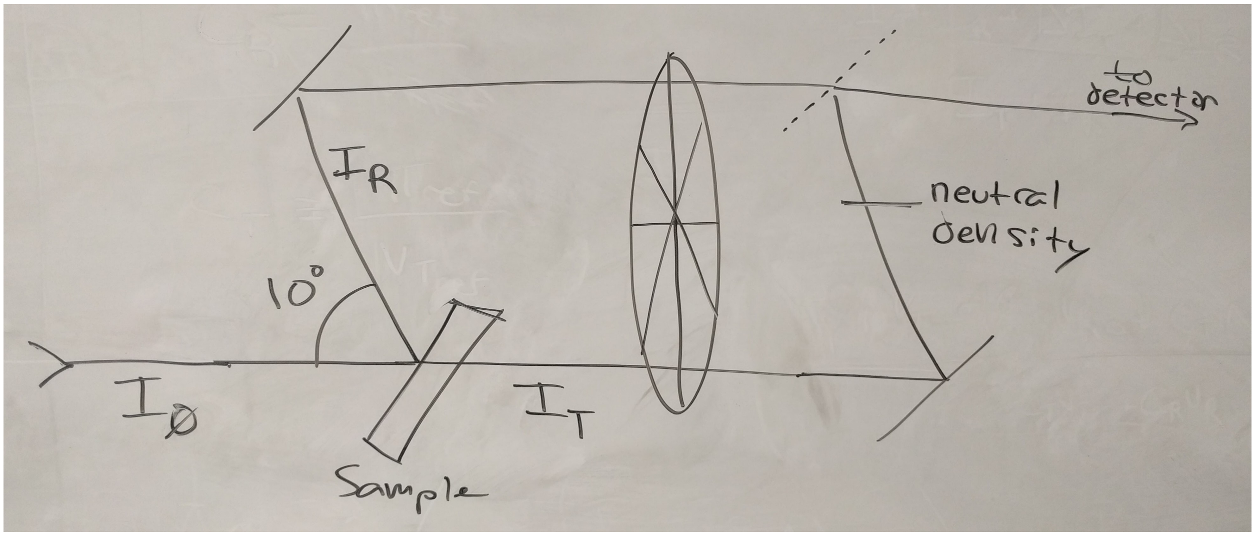

Figure 2.1: CAPTION TODO

2.5.5 Cross Polarized TrEE

2.5.6 Pump-TrEE-Probe

Pump TrEE probe (PTP).

2.6 Instrumental Response Function

The instrumental response function (IRF) is a classic concept in analytical science. Defining IRF becomes complex with instruments as complex as these, but it is still useful to attempt.

It is particularly useful to define bandwidth.

2.6.1 Time Domain

I will use four wave mixing to extract the time-domain pulse-width. I use a driven signal *e.g.* near infrared carbon tetrachloride response. I'll homodyne-detect the output. In my experiment I'm moving pulse 1 against pulses 2 and 3 (which are coincident).

The driven polarization, P, goes as the product of my input pulse *intensities*:

$$P(T) = I_1(t-T) \times I_2(t) \times I_3(t) \tag{2.16}$$

In our experiment we are convolving I_1 with $I_2 \times I_3$. Each pulse has an *intensity-level* width, σ_1, σ_2, and σ_3. $I_2 \times I_3$ is itself a Gaussian, and

$$\begin{aligned} \sigma_{I_2 I_3} &= \ldots && (2.17) \\ &= \sqrt{\frac{\sigma_2^2 \sigma_3^2}{\sigma_2^2 + \sigma_3^2}}. && (2.18) \end{aligned}$$

The width of the polarization (across T) is therefore

$$
\begin{aligned}
\sigma_P &= \sqrt{\sigma_1^2 + \sigma_{I_2 I_3}^2} && (2.19)\\
&= \ldots && (2.20)\\
&= \sqrt{\frac{\sigma_1^2 + \sigma_2^2\sigma_3^2}{\sigma_1^2 + \sigma_2^2}}. && (2.21)
\end{aligned}
$$

I assume that all of the pulses have the same width. I_1, I_2, and I_3 are identical Gaussian functions with FWHM σ. In this case, Equation 2.21 simplifies to

$$
\begin{aligned}
\sigma_P &= \sqrt{\frac{\sigma^2 + \sigma^2\sigma^2}{\sigma^2 + \sigma^2}} && (2.22)\\
&= \ldots && (2.23)\\
&= \sigma\sqrt{\frac{3}{2}} && (2.24)
\end{aligned}
$$

Finally, since we measure σ_P and wish to extract σ:

$$\sigma = \sigma_P\sqrt{\frac{2}{3}} \qquad (2.25)$$

Again, all of these widths are on the *intensity* level.

2.6.2 Frequency Domain

We can directly measure σ (the width on the intensity-level) in the frequency domain using a spectrometer. A tune test contains this information.

2.6.3 Time-Bandwidth Product

For a Gaussian, approximately 0.441

Chapter 3

Materials

"Kroemer's Lemma of Proven Ignorance": If, in discussing a semiconductor problem, you cannot draw an Energy Band Diagram, this shows that you don't know what you are talking about, If you can draw one, but don't, then your audience won't know what you are talking about.

Part II

Instrumental Development

Chapter 4

Software

Cutting-edge science increasingly relies on custom software. In their 2008 survey, Hannay et al. [7] demonstrated just how important software is to the modern scientist.

→ 84.3% of surveyed scientists state that developing scientific software is important or very important for their own research.

→ 91.2% of surveyed scientists state that using scientific software is important or very important for their own research.

→ On average, scientists spend approximately 40% of their work time using scientific software.

→ On average, scientists spend approximately 30% of their work time developing scientific software.

Despite the importance of software to science and scientists, most scientists are not familiar with basic software engineering concepts. This is in part due to the their general lack of formal training in programming and software development. Hannay et al. [7] found that over 90% of scientists learn software development through 'informal self study'. Indeed, I myself have never been formally trained in software development.

Software development in a scientific context poses unique challenges. Many traditional software development paradigms demand an upfront articulation of goals and requirements. This allows the developers to carefully design their software, even before a single line of code is written. In her seminal 2005 case study Segal [8] describes a collaboration between a team of researchers and a contracted team of software engineers. Ultimately

4.1 Overview

In the Wright Group, PyCMDS replaces the old acquisition softwares ‘ps control’, written by Kent Meyer and ‘Control for Lots of Research in Spectroscopy’ written by Schuyler Kain.

4.2 WrightTools

WrightTools is a software package at the heart of all work in the Wright Group.

4.3 PyCMDS

PyCMDS directly addresses the hardware during experiments.

4.3.1 Overview

PyCMDS has, through software improvements alone, dramatically lessened scan times...

→ simultaneous motor motion

→ digital signal processing

→ ideal axis positions 4.3.2

4.3.2 Ideal Axis Positions

Frequency domain multidimensional spectroscopy is a time-intensive process. A typical pixel takes between one-half second and three seconds to acquire. Depending on the exact hardware being scanned and signal being detected, this time may be mostly due to hardware motion or signal collection. Due to the curse of dimensionality, a typical three-dimensional CMDS experiment contains roughly 100,000 pixels. CMDS hardware is transiently-reliable, so speeding up experiments is a crucial component of unlocking ever larger dimensionalities and higher resolutions.

One obvious way to decrease the scan-time is to take fewer pixels. Traditionally, multidimensional scans are done with linearly arranged points in each axis—this is the simplest configuration to program into the acquisition software. Because signal features are often sparse or slowly varying (especially so in high-dimensional scans) linear stepping means that *most of the collected pixels* are duplicates or simply noise. A more intelligent choice of axis points can capture the same nonlinear spectrum in a fraction of the total pixel count.

An ideal distribution of pixels is linearized in *signal*, not coordinate. This means that every signal level (think of a contour in the N-dimensional case) has roughly the same number of pixels defining it. If some generic multidimensional signal goes between 0 and 1, one would want roughly 10% of the pixels to be between 0.9 and 1.0, 10% between 0.8 and 0.9 and so on. If the signal is sparse in the space explored (imagine a narrow two-dimensional Lorentzian in the center of a large 2D-Frequency scan) this would place the majority of the pixels near the narrow peak feature(s), with only a few of them defining the large (in axis space) low-signal floor. In contrast linear stepping would allocate the vast majority of the pixels in the low-signal 0.0 to 0.1 region, with only a few being used to capture the narrow peak feature. Of course, linearizing pixels in signal requires prior expectations about the shape of the multidimensional signal—linear stepping is still an appropriate choice for low-resolution "survey" scans.

CMDS scans often posses correlated features in the multidimensional space. In order to capture such features as cheaply as possible, one would want to define regions of increased pixel density along the correlated (diagonal) lineshape. As a concession to reasonable simplicity, our acquisition software

(PyCMDS) assumes that all scans constitute a regular array with-respect-to the scanned axes. We can acquire arbitrary points along each axis, but not for the multidimensional scan. This means that we cannot achieve strictly ideal pixel distributions for arbitrary datasets. Still, we can do much better than linear spacing.

Almost all CMDS lineshapes (in frequency and delay) can be described using just a few lineshape functions:

→ exponential
→ Gaussian
→ Lorentzian
→ bimolecular

Exponential and bimolecular dynamics fall out of simple first and second-order kinetics (I will ignore higher-order kinetics here). Gaussians come from our Gaussian pulse envelopes or from normally-distributed inhomogeneous broadening. The measured line-shapes are actually convolutions of the above. I will ignore the convolution except for a few illustrative special cases. More exotic lineshapes are possible in CMDS—quantum beating and breathing modes, for example—I will also ignore these. Derivations of the ideal pixel positions for each of these lineshapes appear below.

4.3.3 Exponential

Simple exponential decays are typically used to describe population and coherence-level dynamics in CMDS. For some generic exponential signal S with time constant τ,

$$S(t) = \mathrm{e}^{-\frac{t}{\tau}} . \tag{4.1}$$

We can write the conjugate equation to 4.1, asking “what t do I need to get a certain signal level?”:

$$\log(S) = -\frac{t}{\tau} \tag{4.2}$$

$$t = -\tau \log(S). \tag{4.3}$$

So to step linearly in t, my step size has to go as $-\tau \log(S)$.

We want to go linearly in signal, meaning that we want to divide S into even sections. If S goes from 0 to 1 and we choose to acquire N points,

$$t_n = -\tau \log\left(\frac{n}{N}\right). \tag{4.4}$$

Note that t_n starts at long times and approaches zero delay. So the first t_1 is the smallest signal and t_N is the largest.

Now we can start to consider realistic cases, like where τ is not quite known and where some other longer dynamics persist (manifested as a static offset). Since these values are not separable in a general system, I'll keep S normalized between 0 and 1.

$$S = (1-c)\,\mathrm{e}^{-\frac{t}{\tau_{\text{actual}}}} + c \tag{4.5}$$

$$S_n = (1-c)\,\mathrm{e}^{-\frac{-\tau_{\text{step}}\log\left(\frac{n}{N}\right)}{\tau_{\text{actual}}}} + c \tag{4.6}$$

$$S_n = (1-c)\,\mathrm{e}^{-\frac{\tau_{\text{step}}}{\tau_{\text{actual}}}\log\left(\frac{N}{n}\right)} + c \tag{4.7}$$

$$S_n = (1-c)\left(\frac{N}{n}\right)^{-\frac{\tau_{\text{step}}}{\tau_{\text{actual}}}} + c \tag{4.8}$$

$$S_n = (1-c)\left(\frac{n}{N}\right)^{\frac{\tau_{\text{step}}}{\tau_{\text{actual}}}} + c \tag{4.9}$$

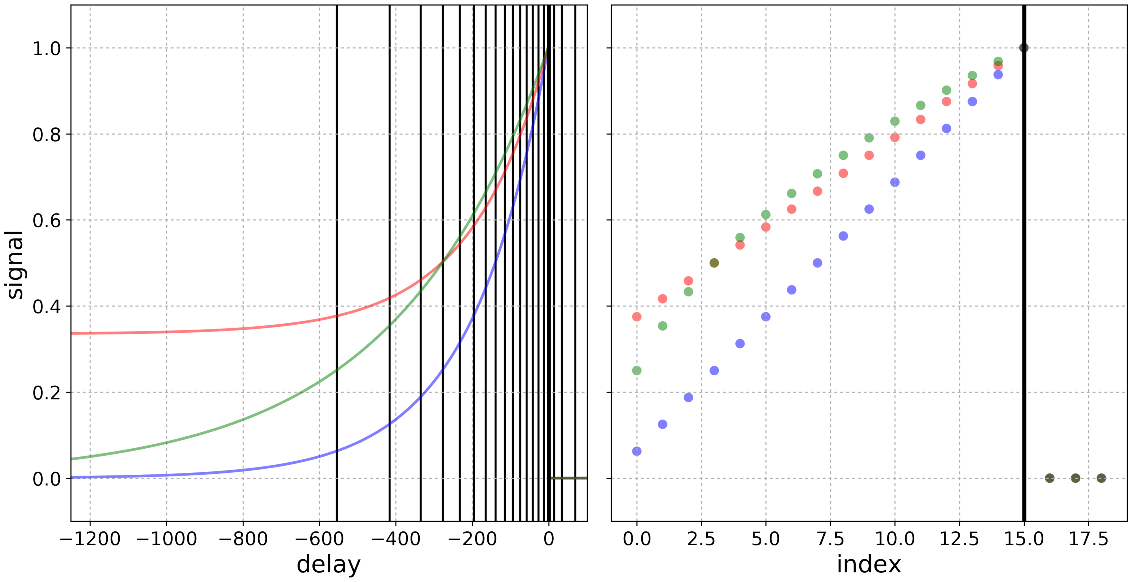

Figure 4.1: TODO

Gaussian

Lorentzian

Bimolecular

4.4 WrightSim

WrightSim does simulations.

Chapter 5

Instrumental Development

5.1 Hardware

5.1.1 Delay Stages

5.2 Signal Acquisition

Old boxcar: 300 ns window, 10 micosecond delay. Onset of saturation 2 V.

5.2.1 Digital Signal Processing

5.3 Artifacts and Noise

5.3.1 Scatter

Scatter is a complex microscopic process whereby light traveling through a material elastically changes its propagation direction. In CMDS we use propagation direction to isolate signal. Scattering samples defeat this isolation step and allow some amount of excitation light to reach the detector. In homodyne-detected 4WM experiments,

$$I_{\text{detected}} = |E_{\text{4WM}} + E_1 + E_2 + E_{2'}|^2 \tag{5.1}$$

Where E is the entire time-dependent complex electromagnetic field. When expanded, the intensity will be composed of diagonal and cross terms:

$$\begin{aligned} I_{\text{detected}} = \overline{(E_1 + E_2)}E_{2'} + (E_1 + E_2)\overline{E_{2'}} + |E_1 + E_2|^2 + (E_1 + E_2)\overline{E_{\text{4WM}}} \\ +(E_1 + E_2)\overline{E_{\text{4WM}}} + \overline{E_{2'}}E_{\text{4WM}} + E_{2'}\overline{E_{\text{4WM}}} + |E_{\text{4WM}}|^2 \end{aligned} \tag{5.2}$$

A similar expression in the case of heterodyne-detected 4WM is derived by Brixner et al. [9]. The goal of any ‘scatter rejection’ processing procedure is to isolate $|E_{\text{4WM}}|^2$ from the other terms.

Abandon the Random Phase Approximation

Interference Patterns in TrEE

TrEE is implicitly homodyne-detected. Scatter from excitation fields will interfere on the amplitude level with TrEE signal, causing interference patterns that beat in delay and frequency space. The pattern of beating will depend on which excitation field(s) reach(es) the detector, and the parameterization of delay space chosen.

First I focus on the interference patterns in 2D delay space where all excitation fields and the detection field are at the same frequency.

Here I derive the slopes of constant phase for the old delay space, where $\text{d1} = \tau_{2'1}$ and $\text{d2} = \tau_{21}$. For simplicity, I take τ_1 to be 0, so that $\tau_{21} \rightarrow \tau_2$ and $\tau_{2'1} \rightarrow \tau_{2'}$. The phase of signal is then

$$\Phi_{\text{sig}} = \mathrm{e}^{-((\tau_{2'} - \tau_2)\omega)} \tag{5.3}$$

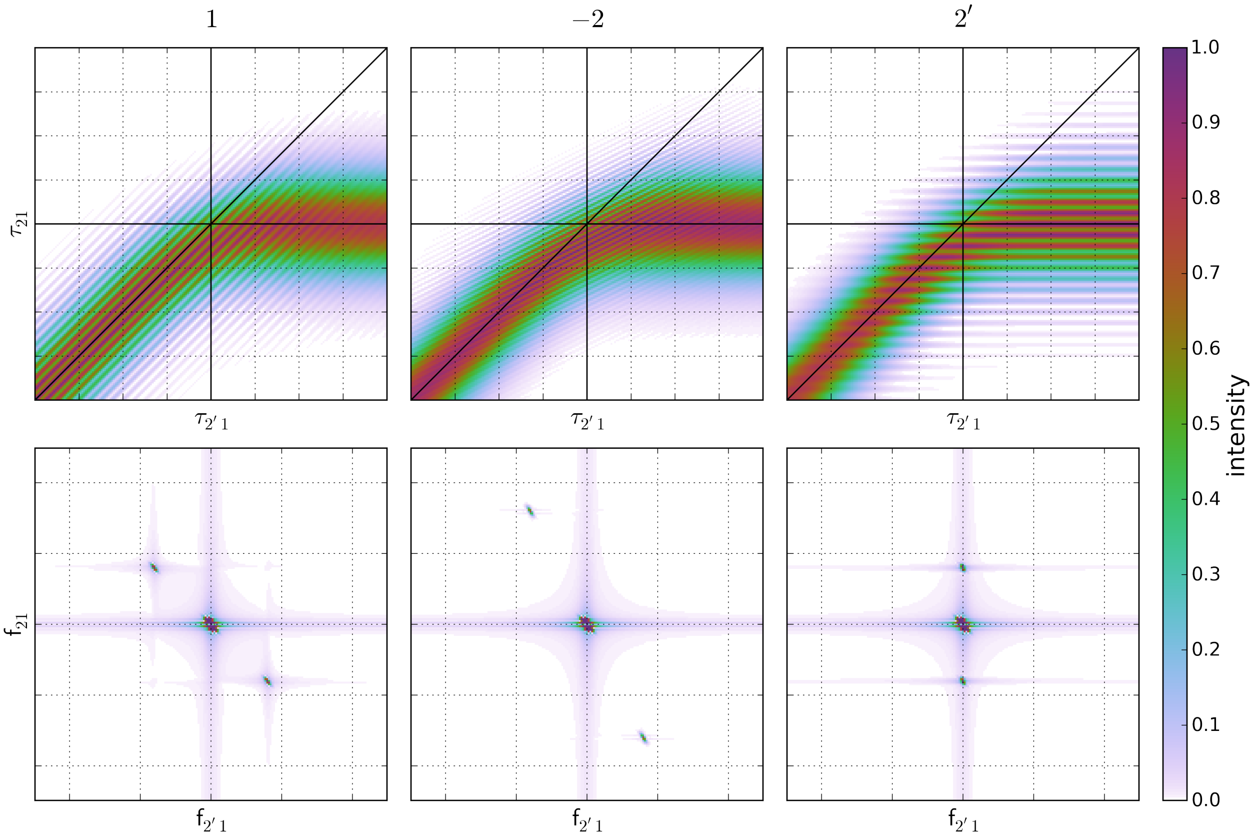

Figure 5.1: Numerically simulated interference patterns between scatter and TrEE for the old delay parametrization. Each column has scatter from a single excitation field. The top row shows the measured intensities, the bottom row shows the 2D Fourier transform, with the colorbar's dynamic range chosen to show the cross peaks.

The phase of each excitation field can also be written:

$$\begin{aligned} \Phi_1 &= e^0 && (5.4) \\ \Phi_2 &= e^{-\tau_2 \omega} && (5.5) \\ \Phi_{2'} &= e^{-\tau_{2'} \omega} && (5.6) \end{aligned}$$

The cross term between scatter and signal is the product of Φ_{sig} and $\Phi_{scatter}$. The cross terms are:

$$\begin{aligned} \Delta_1 = \Phi_{sig} &= e^{-((\tau_{2'} - \tau_2)\omega)} && (5.7) \\ \Delta_2 = \Phi_{sig} e^{-\tau_2 \omega} &= e^{-((\tau_{2'} - 2\tau_2)\omega)} && (5.8) \\ \Delta_{2'} = \Phi_{sig} e^{-\tau_{2'} \omega} &= e^{-\tau_2 \omega} && (5.9) \end{aligned}$$

Figure 5.1 presents numerical simulations of scatter interference as a visual aid. See Yurs 2011 [10].

Here I derive the slopes of constant phase for the current delay space, where $d1 = \tau_{22'}$ and $d2 = \tau_{21}$. I take τ_2 to be 0, so that $\tau_{22'} \rightarrow \tau_{2'}$ and $\tau_{21} \rightarrow \tau_1$. The phase of the signal is then

$$\Phi_{sig} = e^{-((\tau_{2'} + \tau_1)\omega)} \qquad (5.10)$$

The phase of each excitation field can also be written:

$$\begin{aligned} \Phi_1 &= e^{-\tau_1 \omega} && (5.11) \\ \Phi_2 &= e^0 && (5.12) \\ \Phi_{2'} &= e^{-\tau_{2'} \omega} && (5.13) \end{aligned}$$

The cross term between scatter and signal is the product of Φ_{sig} and $\Phi_{scatter}$. The cross terms are:

$$\begin{aligned} \Delta_1 = \Phi_{sig} e^{-\tau_1 \omega} &= e^{-\tau_{2'} \omega} && (5.14) \\ \Delta_2 = \Phi_{sig} &= e^{-((\tau_2 + \tau_1)\omega)} && (5.15) \\ \Delta_{2'} = \Phi_{sig} e^{-\tau_{2'} \omega} &= e^{-\tau_1 \omega} && (5.16) \end{aligned}$$

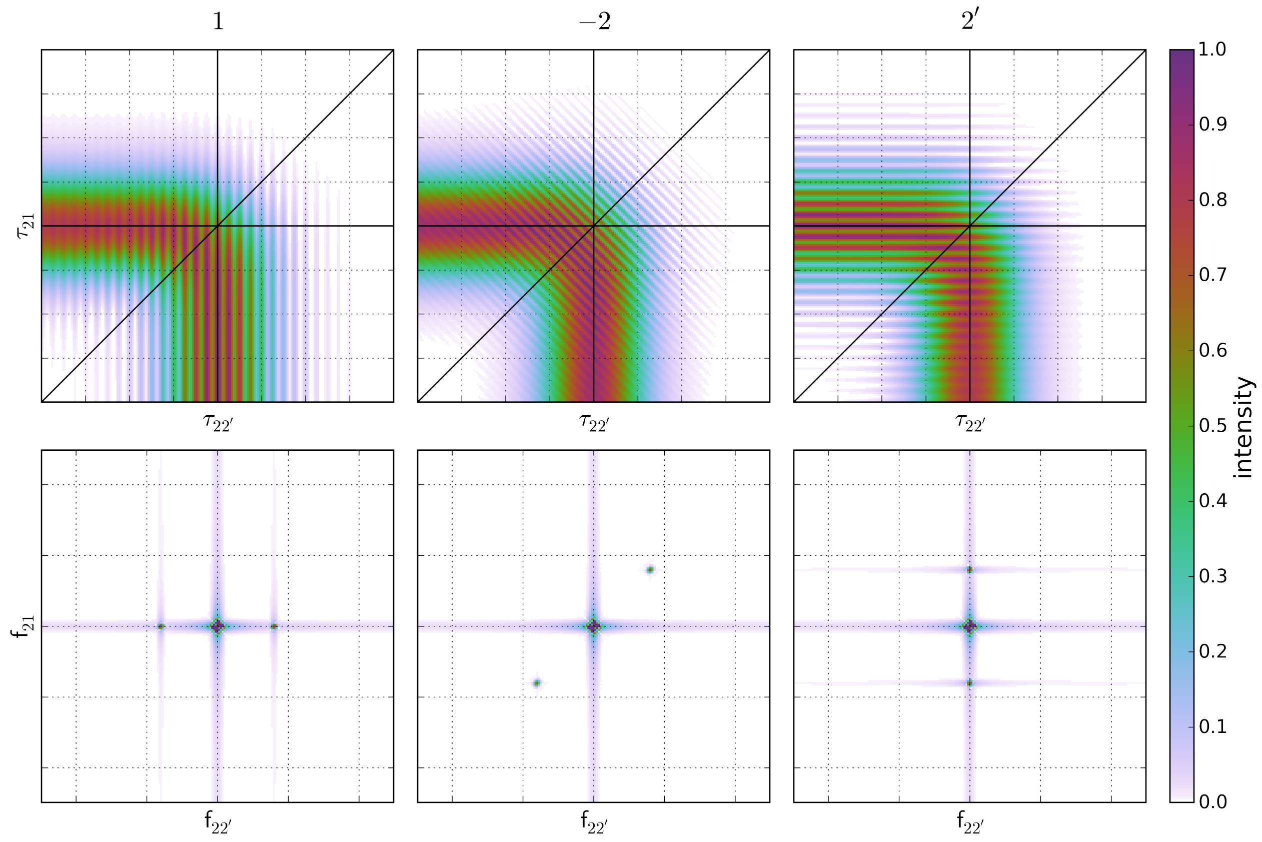

Figure 5.2: Numerically simulated interference patterns between scatter and TrEE for the current delay parametrization. Each column has scatter from a single excitation field. The top row shows the measured intensities, the bottom row shows the 2D Fourier transform, with the colorbar's dynamic range chosen to show the cross peaks.

Figure 5.2 presents numerical simulations of scatter interference for the current delay parameterization.

Instrumental Removal of Scatter

The effects of scatter can be entirely removed from CMDS signal by combining two relatively straightforward instrumental techniques: *chopping* and *fibrillation*. Conceptually, chopping removes intensity-level offset terms and fibrillation removes amplitude-level interference terms. Both techniques work by modulating signal and scatter terms differently so that they may be separated after light collection.

	A	B	C	D
signal			✓	
scatter 1		✓	✓	
scatter 2			✓	✓
other	✓	✓	✓	✓

Table 5.1: Four shot-types in a general phase shifted parallel modulation scheme. The 'other' category represents anything that doesn't depend on either chopper, including scatter from other excitation sources, background light, detector voltage offsets, etc.

We use the dual chopping scheme developed by Furuta, Fuyuki, and Wada [11] called 'phase shifted parallel modulation'. In this scheme, two excitation sources are chopped at 1/4 of the laser repetition rate (two pulses on, two pulses off). Very similar schemes are discussed by Augulis and Zigmantas [12] and Heisler et al. [13] for two-dimensional electronic spectroscopy. The two chop patterns are phase-shifted to make the four-pulse pattern represented in Table 5.1. In principle this chopping scheme can be achieved with a single judiciously placed mechanical chopper - this is one of the advantages of Furuta's scheme. Due to practical considerations we have generally used two choppers, one on each OPA. The key to phase shifted parallel modulation is that signal only appears when both of your chopped beams are passed. It is simple to show how signal can be separated through simple addition and subtraction of the A, B, C, and D phases shown in Table 5.1. First, the components of each phase:

$$A = I_{\text{other}} \tag{5.17}$$

$$B = I_1 + I_{\text{other}} \tag{5.18}$$

$$C = I_{\text{signal}} + I_1 + I_2 + I_{\text{other}} \tag{5.19}$$

$$D = I_2 + I_{\text{other}} \tag{5.20}$$

Grouping into difference pairs,

$$A - B = -I_1 \tag{5.21}$$

$$C - D = I_{\text{signal}} + I_1 \tag{5.22}$$

So:

$$A - B + C - D = I_{\text{signal}} \tag{5.23}$$

I have ignored amplitude-level interference terms in this treatment because they cannot be removed via any chopping strategy. Interference between signal and an excitation beam will only appear in 'C'-type shots, so it will not be removed in Equation 5.23. To remove such interference terms, you must *fibrillate* your excitation fields.

An alternative to dual chopping is single-chopping and 'leveling'... this technique was used prior to May 2016 in the Wright Group... 'leveling' and single-chopping is also used in some early 2DES work... [9].

Figure 5.3 shows the effects of dual chopping for some representative MoS_2 TA data. Each subplot is a probe wigner, with the vertical grey line representing the pump energy. Note that the single chopper passes pump scatter, visible as a time-invariant increase in intensity when the probe and monochromator are near the pump energy. Dual chopping efficiently removes pump scatter, but at the cost of signal to noise for the same number of laser shots. Taking twice as many laser shots when dual chopping brings the signal to noise to at least as good as the original single chopping.

Fibrillation is the intentional randomization of excitation phase during an experiment. Because the interference term depends on the phase of the excitation field relative to the signal, averaging over many shots with random phase will cause the interference term to approach zero. This is a well known strategy for removing unwanted interference terms [14, 15].

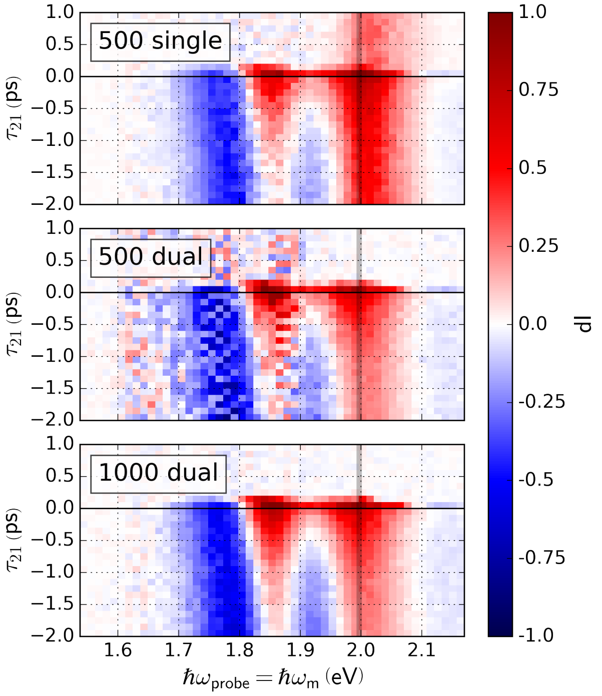

Figure 5.3: Comparison of single and dual chopping in a MoS_2 transient absorption experiment. Note that this data has not been processed in any way - the colorbar represents changes in intensity seen by the detector. The grey line near 2 eV represents the pump energy. The inset labels are the number of laser shots taken and the chopping strategy used.

5.3.2 Normalization of dual-chopped self-heterodyned signal

Shot-by-shot normalization is not trivial for these experiments. As in table above, with 1 as pump and 2 as probe.

Starting with ΔI from 5.23, we can normalize by probe intensity to get the popular $\Delta I/I$ representation. Using the names defined above:

$$\frac{\Delta I}{I} = \frac{A - B + C - D}{D - A} \tag{5.24}$$

Now consider the presence of excitation intensity monitors, indicated by subscripts PR for probe and PU for pump.

We can further normalize by the pump intensity by dividing the entire expression by C_{PU}:

$$\frac{\Delta I}{I} = \frac{A - B + C - D}{(D - A) * C_{PU}} \tag{5.25}$$

Now, substituting in BRAZARD formalism:

$$\begin{aligned}
A &= constant && (5.26)\\
B &= SI^{B}_{PU}(1 + \delta^{B}_{PU}) && (5.27)\\
C &= I^{C}_{PR}(1 + \delta^{C}_{PR}) + SI^{C}_{PU}(1 + \delta^{C}_{PR}) && (5.28)\\
D &= I^{D}_{PR}(1 + \delta^{D}_{PR}) && (5.29)
\end{aligned}$$

$$\frac{\Delta I}{I} = \frac{< A > - \frac{<B_{PU}>B}{B_{PU}} + \frac{<C_{PU}><C_{PR}C}{C_{PU}C_{PR}} - \frac{<D_{PR}>D}{D_{PR}}}{< PR >< PU >} \tag{5.30}$$

5.4 Light Generation

5.4.1 Automated OPA Tuning

5.5 Optomechanics

5.5.1 Automated Neutral Density Wheels

Part III

Applications

Chapter 6

PbSe

Chapter 7

MX2

We report the first coherent multidimensional spectroscopy study of a MoS_2 film. A four-layer sample of MoS_2 was synthesized on a silica substrate by a simplified sulfidation reaction and characterized by absorption and Raman spectroscopy, atomic force microscopy, and transmission electron microscopy. State-selective coherent multidimensional spectroscopy (CMDS) on the as-prepared MoS_2 film resolved the dynamics of a series of diagonal and cross-peak features involving the spin—orbit split A and B excitonic states and continuum states. The spectra are characterized by striped features that are similar to those observed in CMDS studies of quantum wells where the continuum states contribute strongly to the initial excitation of both the diagonal and cross-peak features, while the A and B excitonic states contributed strongly to the final output signal. The strong contribution from the continuum states to the initial excitation of both the diagonal and cross-peak features, while the A and B excitonic states contributed strongly to the final output signal. The strong contribution from the continuum states to the initial excitation shows that the continuum states are coupled to the A and B excitonic states and that fast intraband relaxation is occurring on a sub-70 fs time scale. A comparison of the CMDS excitation signal and the absorption spectrum shows that the relative importance of the continuum states is determined primarily by their absorption strength. Diagonal and cross-peak features decay with a 680 fs time constant characteristic of exciton recombination and/or trapping. The short time dynamics are complicated by coherent and partially coherent pathways that become important when the excitation pulses are temporally overlapped. In this region, the coherent dynamics create diagonal features involving both the excitonic states and continuum states, while the partially coherent pathways contribute to cross-peak features.

7.1 Introduction

Transition metal dichalcogenides (TMDCs), such as MoS_2, are layered semiconductors with strong spin-orbit coupling, high charge mobility, and an indirect band gap that becomes direct for monolayers. [16, 17] The optical properties are dominated by the A and B excitonic transitions between two HOMO spin-orbit split valence bands and the lowest state of the conduction band at the K and K' valleys of the two-dimensional hexagonal Brillouin zone. [18] The spin and valley degrees of freedom are coupled in individual TMDC layers as a result of the strong spin-orbit coupling and the loss of inversion symmetry. The coupling suppresses spin and valley relaxation since both spin and valley must change in a transition. These unusual properties have motivated the development of TMDC monolayers for next-generation nano/optoelectronic devices as well as model systems for spintronics and valleytronics applications. [17, 19, 20]

Ultrafast dynamics of the MoS_2 A and B electronic states have been measured by pump-probe, transient absorption, and transient reflection spectroscopy. [21, 4, 22, 23, 24] The spectra contain A and B excitonic features that result from ground-state bleaching (GSB), stimulated emission (SE), and excited-state absorption (ESA) pathways. The excitons exhibit biexponential relaxation times of $\approx$10–20 and $\approx$350–650 fs, depending on the fluence and temperature. The dependence on excitation frequency has not been explored in previous ultrafast experiments on MoS_2, but it has played a central role in understanding exciton cooling dynamics and exciton-phonon coupling in studies of quantum dots. [25]

Coherent multidimensional spectroscopy (CMDS) is a complementary four wave mixing (FWM) methodology that differs from pump-probe, transient absorption, and transient reflection methods. [20, 21, 4, 22, 24, 26, 23] Rather than measuring the intensity change of a probe beam caused by the state population changes induced by a pump beam, CMDS measures the intensity of a coherent output beam created by interactions with three excitation pulses. The interest in CMDS methods arise from their ability to remove inhomogeneous broadening, define interstate coupling, and resolve coherent and incoherent dynamics. [27, 28, 29, 10, 30, 31, 32, 33, 34] CMDS typically requires interferometric phase stability between excitation pulses, so CMDS has been limited to materials with electronic states within the excitation-pulse bandwidth. Multiresonant CMDS is a particularly attractive method for the broader range of complex materials because it does not require interferometric stability and is able to use independently tunable excitation pulses over wide frequency ranges.

The multiresonant CMDS used in this work employs two independently tunable excitation beams with frequencies ω_1 and ω_2. The ω_2 beam is split into two beams, denoted by ω_2 and ω_2'. These three beams are focused onto the MoS$_2$ thin film at angles, creating an output beam in the phase-matched direction $\mathbf{k}_{\text{out}} = \mathbf{k}_1 - \mathbf{k}_2 + \mathbf{k}_{2'}$ where $\mathbf{k}$ is the wave vector for each beam and the subscripts label the excitation frequencies. Multidimensional spectra result from measuring the output intensity dependence on frequency and delay times.

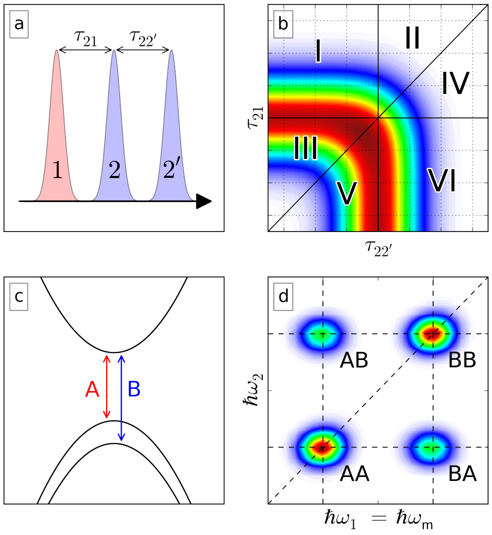

Figure 7.1: (a) Example delays of the ω_1, ω_2, and $\omega_{2'}$ excitation pulses. (b) Dependence of the output intensity on the $\tau_{22'}$ and τ_{21} time delays for $\omega_1 = \omega_2$. The solid lines define the regions for the six different time orderings of the ω_1, ω_2, and $\omega_{2'}$ excitation pulses. We have developed a convention for numbering these time orderings, as shown. (c) Diagram of the band structure of MoS$_2$ at the K point. The A and B exciton transitions are shown. (d) Two dimensional frequency-frequency plot labeling two diagonal and cross-peak features for the A and B excitons.

Figure 7.1 introduces our conventions for representing multidimensional spectra. Figure 7.1b,d are simulated data. Figure 7.1a shows one of the six time orderings of the three excitation pulses where

$\tau_{22'} \equiv t_2 - t_{2'} > 0$ and $\tau_{21} \equiv t_2 - t_1 < 0$; that is, the $\omega_{2'}$ pulse interacts first and the ω_1 pulse interacts last. Figure 7.1b illustrates the 2D delay-delay spectrum for all six time orderings when ω_1 and ω_2 are both resonant with the same state. The color denotes the output amplitude. Along the negative ordinate where $\tau_{22'} = 0$, interactions with the ω_2 and $\omega_{2'}$ pulses create a population that is probed by ω_1. Similarly, along the negative absicissa where $\tau_{21} = 0$, interactions with the ω_2 and ω_1 pulses create a population that is probed by $\omega_{2\prime}$. The decay along these axes measures the population relaxation dynamics. Note that these delay representations differ from previous publications by our group. [35] This paper specifically explores the dynamics along the ordinate where $\tau_{22'}$ is zero and the τ_{21} delay is changed.

Figure 7.1c depicts the A and B excitonic transitions between the spin-orbit split valence bands and the degenerate conduction band states of MoS_2. Figure 7.1d illustrates the 2D frequency-frequency spectrum when ω_1 and ω_2 are scanned over two narrow resonances. The spectrum contains diagonal and cross-peaks that we label according to the excitonic resonances AA, AB BA, and BB for illustrative purposes. The dynamics of the individual quantum states are best visualized by 2D frequency-delay plots, which combine the features seen in Figure 7.1b,d.

This works reports the first multiresonant CMDS spectra of MoS_2. It includes the excitation frequency dependence of the A and B excitonic-state dynamics. These experiments provide a fundamental understanding of the multidimensional MoS_2 spectra and a foundation for interpreting CMDS experiments on more complex TMDC heterostructures. The experimental spectra differ from the simple 2D spectrum shown in Figure 7.1d and those of earlier CMDS experiments with model systems. The line shape of the CMDS excitation spectrum closely matches the absorption spectrum, but the line shape of the output coherence is dominated by the A and B excitonic features. The difference arises from fast, < 70 fs intraband relaxation from the hot A and B excitons of the continuum to the band edge. A longer, 680 fs relaxation occurs because of trapping and/or exciton dynamics. [24] The intensity of the cross-peaks depends on the importance of state filling and intraband relaxation of hot A excitons as well as the presence of interband population trnasfer of the A and B exciton states.

7.2 Methods

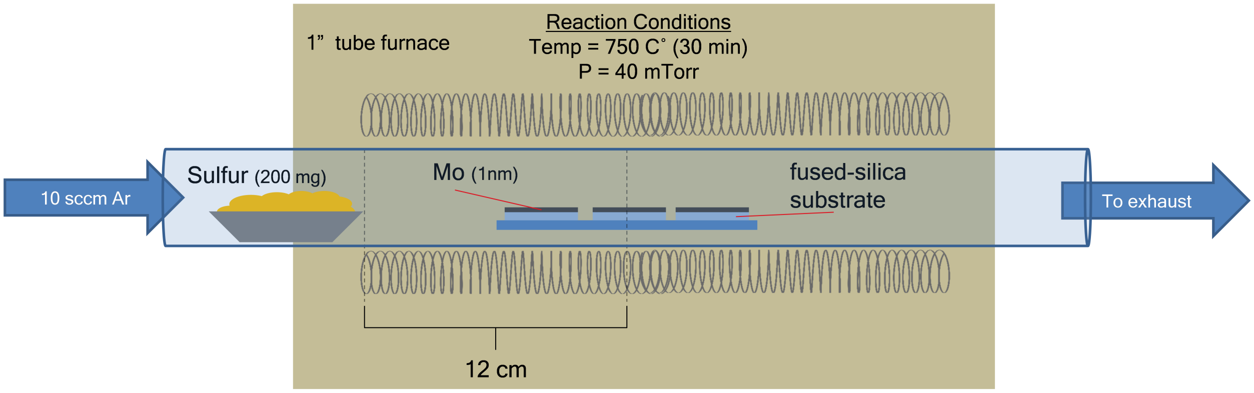

Figure 7.2: Schemiatic of the synthetic setup used for Mo thin film sulfidation reactions.

MoS_2 thin films were prepared *via* a Mo film sulfidation reaction, similar to methods reported by Laskar et al. [36]. A 1 nm amount of Mo (Kurt J. Lesker, 99.95%) metal was electron-beam evaporated onto a fused silica substrate at a rate of 0.05 Å/s. The prepared Mo thin films were quickly transferred to the center of a 1-inch fused silica tub furnace equipped with gas flow controllers (see Figure 7.2) and purged with Ar. The temperature of the Mo substrate was increased to 900 °C over the course of 15 min, after which 200 mg of sulfur was evaporated into the reaction chamber. Sulfidation was carried out for 30 min, and the furnace was subsequently cooled to room temperature; then the reactor tube was returned to atmospheric pressure, and the MoS_2 thin film samples were collected. The MoS_2 samples were characterized and used for CMDS experiments with no further preparation.

MoS_2 thin film absorption spectra were collected by a Shimadzu 2401PC ultraviolet-visible spectrophotometer. Raman and photoluminescence experiments were carried out in parallel using a Thermo DXR Raman microscope with a 100x 0.9 NA focusing objective and a 2.0 mW 532 nm excitation source. Raman/PL measurements were intentionally performed at an excitation power of <8.0 mW to prevent sample damage. [37] Contact-mode atomic foce microscopy was performed with an Agilent 5500 AFM. MoS_2 film thickness was determined by scratching the sample to provide a clean step-edge between the MoS_2 film and the fused silica substrate. TEM samples were prepared following the method outlined by Shanmugam, Durcan, and Yu [38] using concentrated KOH in a 35 °C oil bath for 20 minutes. The delaminated MoS_2 sample was removed from the basic solution, rinsed five times with DI water, and transferred to a Cu-mesh TEM grid. TEM experiments were performed on a FEI Titan aberration corrected (S)TEM under 200 kV accelerating voltage.

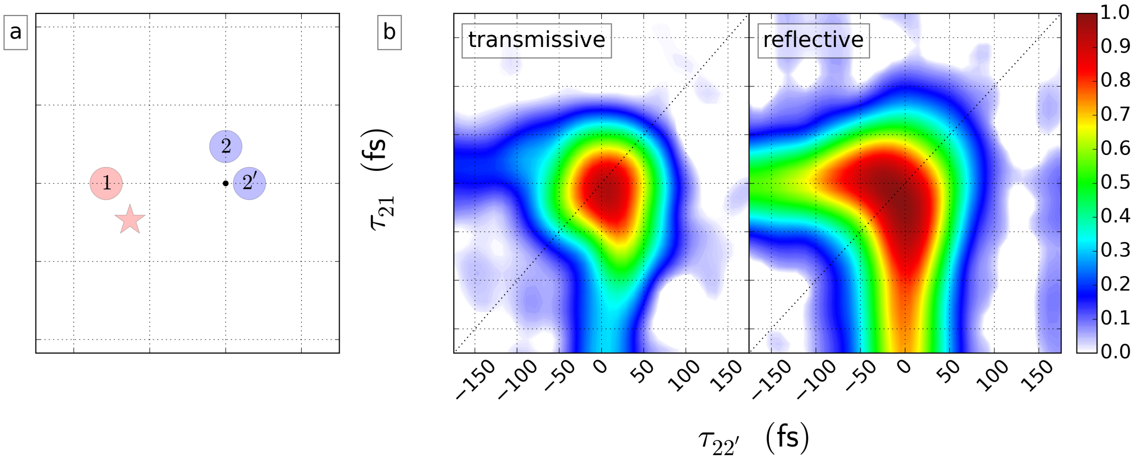

Figure 7.3: (a) Mask. (b) 2D delay spectra at the BB diagonal ($\omega_1 = \omega_2 \approx 1.95$ eV) for transmissive and reflective geometries. Transmissive signal is a mixture of MoS_2 signal and a large amount of driven signal from the substrate that only appears in the pulse overlap region. Reflective signal is representative of the pure MoS_2 response.

The coherent multidimensional spectroscopy system used a 35 fs seed pulse, centered at 800 nm and generated by a 1 kHz Tsunami Ti-sapphire oscillator. The seed was amplified by a Spitfire-Pro regenerative amplifier. The amplified output was split to pump two TOPAS-C collinear optical parametric amplifiers. OPA signal output was immediately frequency doubled with BBO crystals, providing two ≈50 fs independently tunable pulses denoted ω_1 and ω_2 with frequencies ranging from 1.62 to 2.12 eV. Signal and idler were not filtered out, but played no role due to their low photon energy. Pulse ω_2 was split into pulses labeled ω_2 and $\omega_{2'}$ to create a total of three excitation pulses.

In this experiment we use motorized OPAs which allow us to set the output color in software. OPA1 and OPA2 were used to create the ω_1 and ω_2 frequencies, respectively. In Figure 7.4 we compare the spectral envelope generated by the OPA at each set color. Negative detuning values correspond to regions of the envelope lower in energy than the corresponding set color. The colorbar allows for comparison between set color intensities. The fluence values reported correspond to the brightest set color for each OPA. A single trace of OPA2 output at set color = 1.95 eV can be found in Figure 7.7.

After passing through automated delay stages (Newport SMC100 actuators), all three beams were focused onto the sample surface by a 1 meter focal length spherical mirror in a distorted BOXCARS

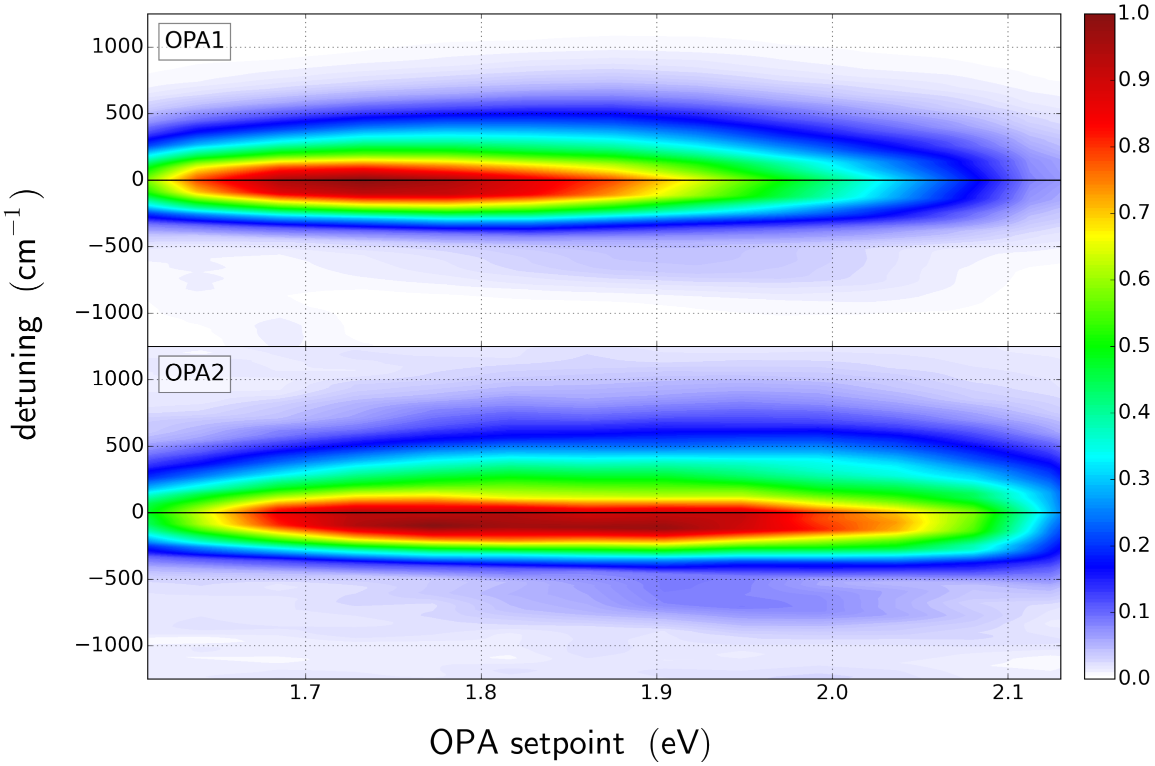

Figure 7.4: OPA outputs at each color explored.

geometry to form a 630, 580, and 580 μm FWHM spot sizes for ω_1, ω_2, and $\omega_{2'}$, respectively.

Figure 7.5 represents delay corrections applied for each OPA. The corrections were experimentally determined using driven FWM output from fused silica. Corrections were approximately linear against photon energy, in agreement with the normal dispersion of transmissive optics inside our OPAs and between the OPAs and the sample. OPA2 required a relatively small correction along $\tau_{22'}$ (middle subplot) to account for any dispersion experienced differently between the two split beams. OPA1 was not split and therefore needed no such correction.

Figure 7.3a represents the to-scale mask that defines our distorted BOXCARS configuration. Relative to the center of the BOXCARS mask (small black dot), ω_1, ω_2, and $\omega_{2'}$ enter the sample at angles of 5.0, 1.5, and 1.0 degrees. Each is angled only along the vertical or horizontal dimension, as indicated in Figure 7.3a. This distortion allowed us to remove a large amount of unwanted ω_2 and $\omega_{2'}$ photons from our signal path (Figure 7.3a red star). ω_1 photons were less efficiently rejected, as we show below.

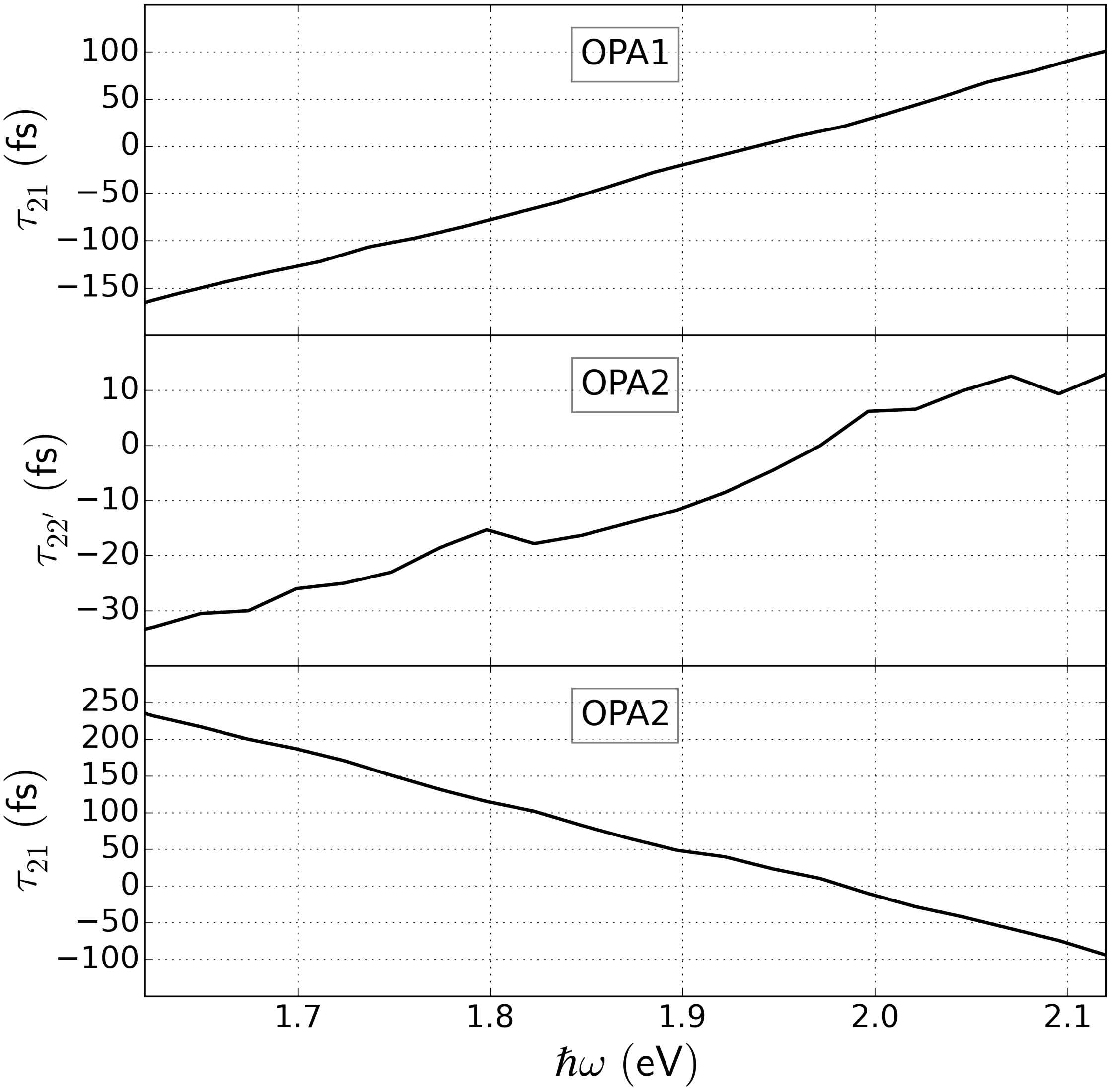

Figure 7.5: Spectral delay correction.

The center of the BOXCARS mask was brought into the sample at ≈45 degrees. All three beams had S polarization. After reflection, the output beam was isolated using a series of apertures, spectrally resolved with a monochromator (spectral resolution 9 meV). and detected using a photomultiplier (RCA C31034A).

Our experimental setup allowed for the collection of both transmissive and reflective (epi-directional) FWM signal. The 2D delay spectra in Figure 7.3b show the presence of a large nonresonant contribution at the origin for the transmissive FWM signal and weaker signals from the MoS_2 thin film at negative values of τ_{21} and $\tau_{22'}$. The nonresonant contribution is much weaker than the signals from the film for the reflective signal id is the geometry chosen for this experiment. This discrimination between a film and the substrate was also seen in reflective and transmissive CARS microscopy experiments. [39]

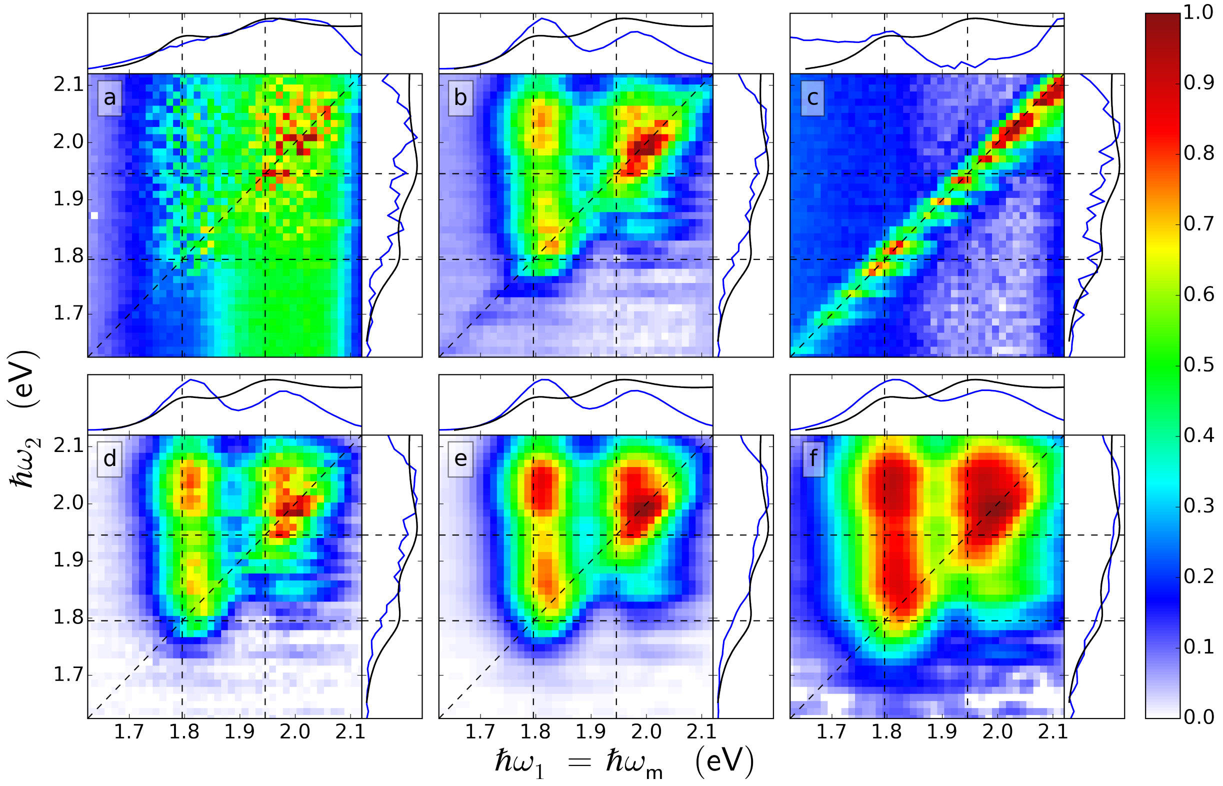

Figure 7.6: Visualization of data collection and processing. With the exception of (c), each subsequent pane represents an additional processing step on top of previous processing. The color bar of each image is separate. (a) Voltages read by the detector at teach color combination. The large vertical feature is ω_1 scatter; the shape is indicative of the power curve of the OPA. MoS_2 response can be barely seen above this scatter. (b) Data after chopping and active background subtraction at the boxcar (100 shots). (c) The portion of chopped signal that is not material response. This portion is extracted by averaging several collections at very positive τ_{21} values, where no material response is present due to the short coherence times of MoS_2 electronic states. The largest feature is ω_2 scatter. Cross-talk between digital-to-analog channels can also be seen as the negative portion that goes as ω_1 intensity. (d) Signal after (c) is subtracted. (e) Smoothed data. (f) Amplitude level (square root) data. This spectrum corresponds to that at 0 delay in Figure 7.9. Note that the color bar's range is different than in Figure 7.9.

Once measured, the FWM signal was sent through a four-stage workup process to create the data set shown here. This workup procedure is visualized in Figure 7.6. We use a chopper and boxcar in active background subtraction mode (averaging 100 laser shots) to extract the FWM signal from ω_1

and ω_2 scatter. We collect this differential signal (Figure 7.6b) in software with an additional 50 shots of averaging. In post-process we subtract ω_2 scatter and smooth the data using a 2D Kaiser window. Finally, we represent the homodyne collected data as $(\text{sig})^{1/2}$ to make the dynamics and line widths comparable to heterodyne-collected techniques like absorbance and pump-probe spectra. Throughout this work, zero signal on the color bar is set to agree with the average rather than the minimum of noise. Values below zero due to measurement uncertainty underflow the color bar and are plotted in white. This is especially evident in lots such as +120 fs in Figure 7.14, where there is no real signal. IPython [40] and matplotlib [41] were important for data processing and plotting in this work.

7.3 Results and discussion

The few-layer MoS_2 thin film sample studied in this work was prepared on a transparent fused silica substrate by a simple sufidation reaction of a Mo thin film using a procedure modified from a recent report. [36] Figure 7.7a and b show the homogeneous deposition and surface smoothness of the sample over the centimeter-sized fused silica substrate, respectively. The Raman spectrum shows the E^1_{2g} and A_{1g} vibrational modes (Figure 7.7c) that are characteristic of MoS_2. [42] The transmission electron micrograph (TEM) in Figure 7.7d shows the lattice fringes of the film with an inset fast Fourier transform (FFT) of the TEM image indicative of the hexagonal crystal structure of the film corresponding to the 0001 plane of MoS_2. [43] The MoS_2 film thickness was determined to be 2.66 nm by atomic force microscopy and corresponds to approximately four monolayers. Figure 7.73 shows the absorption and fluorescence spectrum of the film along with the A and B excitonic line shapes that were extracted from the absorption spectrum. A representative excitation pulse profile is also shown in red for comparison.

Extracting the exciton absorbance spectrum is complicated by the large “rising background” signal from other MoS_2 bands. With this in mind, we fit the second derivative absorption spectrum to a sum of two second derivative Gaussians, as seen in Figure 7.8. Conceptually, this method can be thought of as maximizing the smoothness (as opposed to minimizing the amplitude) of the remainder between the fit and the absorption spectrum. The fit parameters can be found in the inset table in Figure 7.8. The Gaussians themselves and the remainder can be found in Figure 7.8.

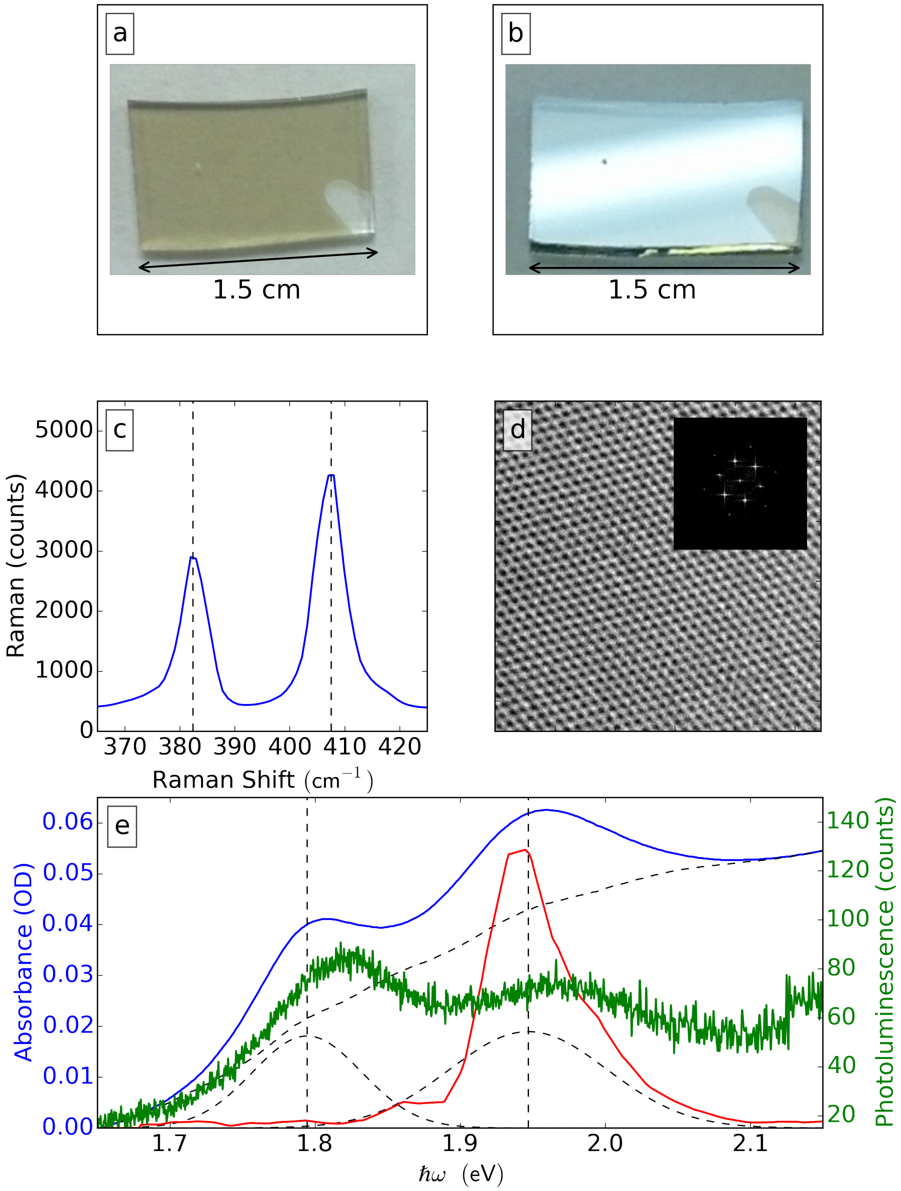

Figure 7.7: Characterization of the few-layer MoS$_2$ film studied in this work. Optical images of the MoS$_2$ thin film on fused silica substrate in (a) transmission and (b) reflection. (c) Raman spectrum of the E^1_{2g} and A_{1g} vibrational modes. (d) High-resolution TEM image and its corresponding FFT shown in the inset. (e) Absorption (blue), photoluminescence (green), Gaussian fits to the A and B excitons, along with the residules betwen the fits and absorbance (dotted), A and B exciton centers (dotted) and representative excitation pulse shape (red).

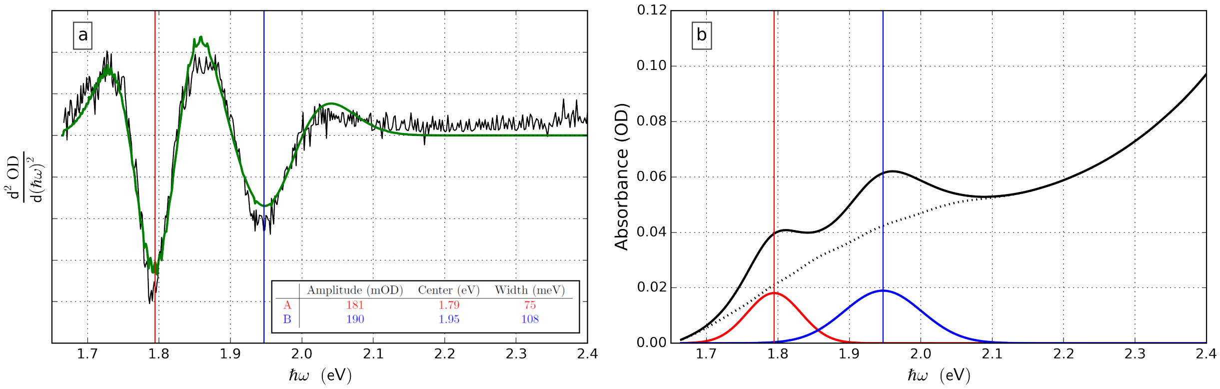

	Amplitude (mOD)	Center (eV)	Width (meV)
A	181	1.79	75
B	190	1.95	108

Figure 7.8: Extraction of excitonic features from absorbance spectrum. (a) Second derivative spectra of absorbance (black) and fit second derivative spectrum (green). Gaussian fit parameters are shown in the inset table. (b) Absorption curve (black), Gaussian fits (blue and red), and remainder (black dotted).

The multiresonant CMDS experiment uses ≈70 fs excitation pulses created by two independently tunable optical parametric amplifiers (OPAs). Automated delay stages and neutral density filters set the excitation time delays over all values of τ_{21} with $\tau_{22'} = 0$ and the pulse fluence to 90 μJ/cm^2 (114 μJ/cm^2) for the ω_1 (ω_2 and $\omega_{2'}$) beam(s). Each pulse was focused onto the sample using a distorted BOXCARS configuration. [44] The FWM signal was spatially isolated and detected with a monochromator that tracks the output frequency so $\omega_m = \omega_1$. In order to compare the FWM spectra with the absorption spectrum, the signal has been defined as the square root of the measured FWM signal since FWM depends quadratically on the sample concentration and path length.

The main set of data presented in this work is an $\omega_1\omega_2\tau_{21}$ "movie" with $\tau_{22'} = 0$. **??** shows representative 2D frequency-frequency slices from this movie at increasingly negative τ_{21} times. Each 2D frequency spectrum contains side plots along both axes that compare the absorbance spectrum (black) to the projection of the integrated signal onto the axis (blue). Along ω_1 (which for negative τ_{21} times acts as the "probe") we observe two peaks corresponding to the A and B excitons. In contrast, we see no well-defined excitonic peaks along the ω_2 "pump" axis. Instead, the signal amplitude increases toward bluer ω_2 values. The decrease in FWM above 2.05 eV is caused by a drop in the ω_2 OPA power.

Figures 7.10 and 7.11 show representative 2D frequency-delay slices from this movie, where the absicissa is the ω_1 or ω_2 frequency, respectively, the ordinate is the τ_{21} delay time, and the solid bold lines represent

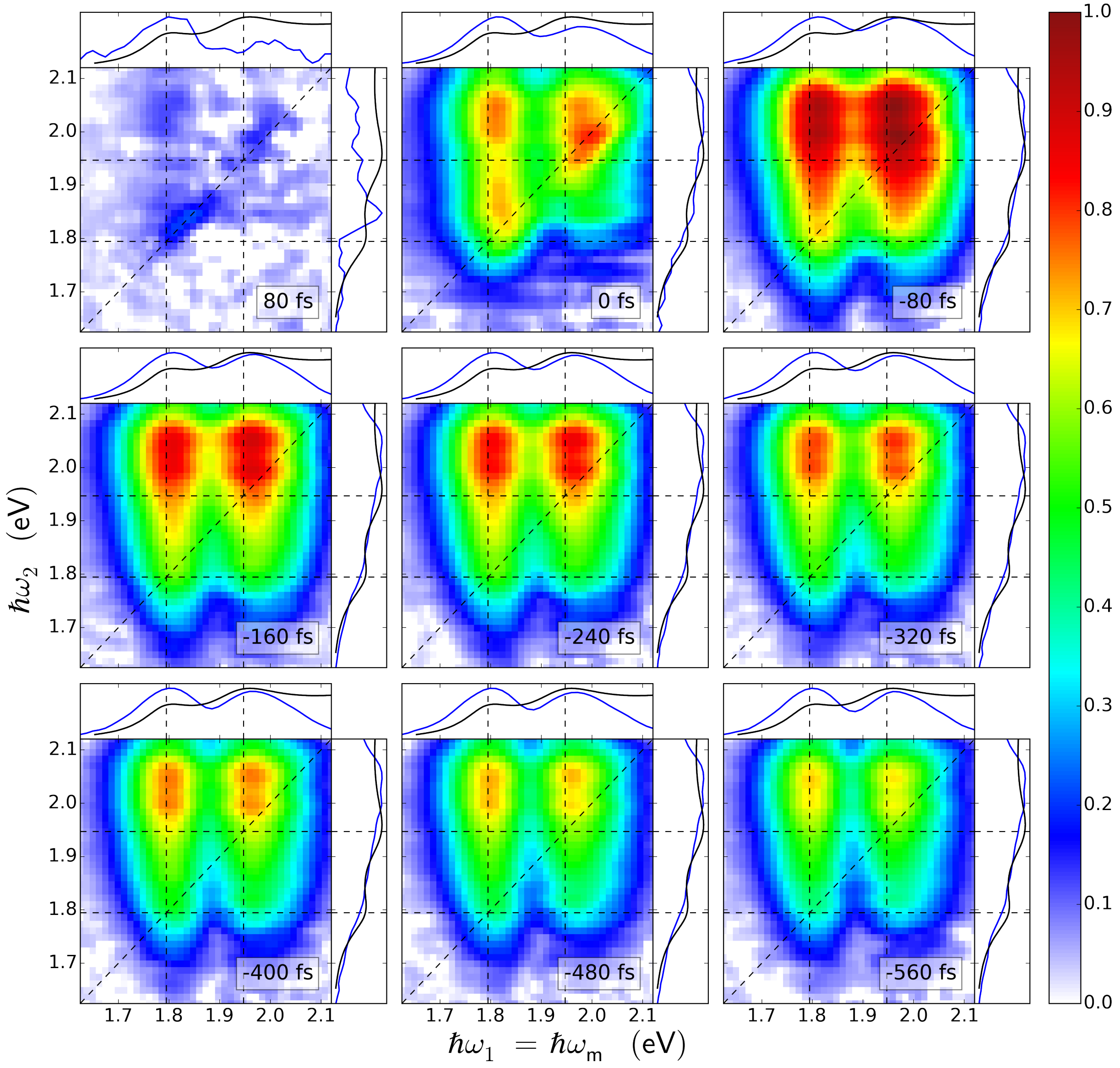

Figure 7.9: 2D frequency-frequency spectra of the MoS_2 sample in the epi configuration. In all spectra $\tau_{22'} = 0$ fs, while τ_{21} is designated in the bottom-right corner of each spectral panel. The color bar defines the square root of the intensity normalized to the most intense feature in the series of spectra. The integration of the signal onto the $\hbar\omega_1 = \hbar\omega_m$ and $\hbar\omega_2$ axes are represented ans the blue curves in the top and right side plots, respectively. The side plots also contain the absorbance spectrum (black line) to aid intepretation of the dynamics of the integrated 2D signals. The dashed lines mark the centers of the A and B excitons, as designated from the absorption spectrum.

five different ω_2 or ω_1 frequencies. The color bar is normalized to the brightest feature in each subplot. This normalization allows comparison of the time dependence of the line shapes, positions, and relative signal amplitudes along the ω_1 or ω_2 axis directly.

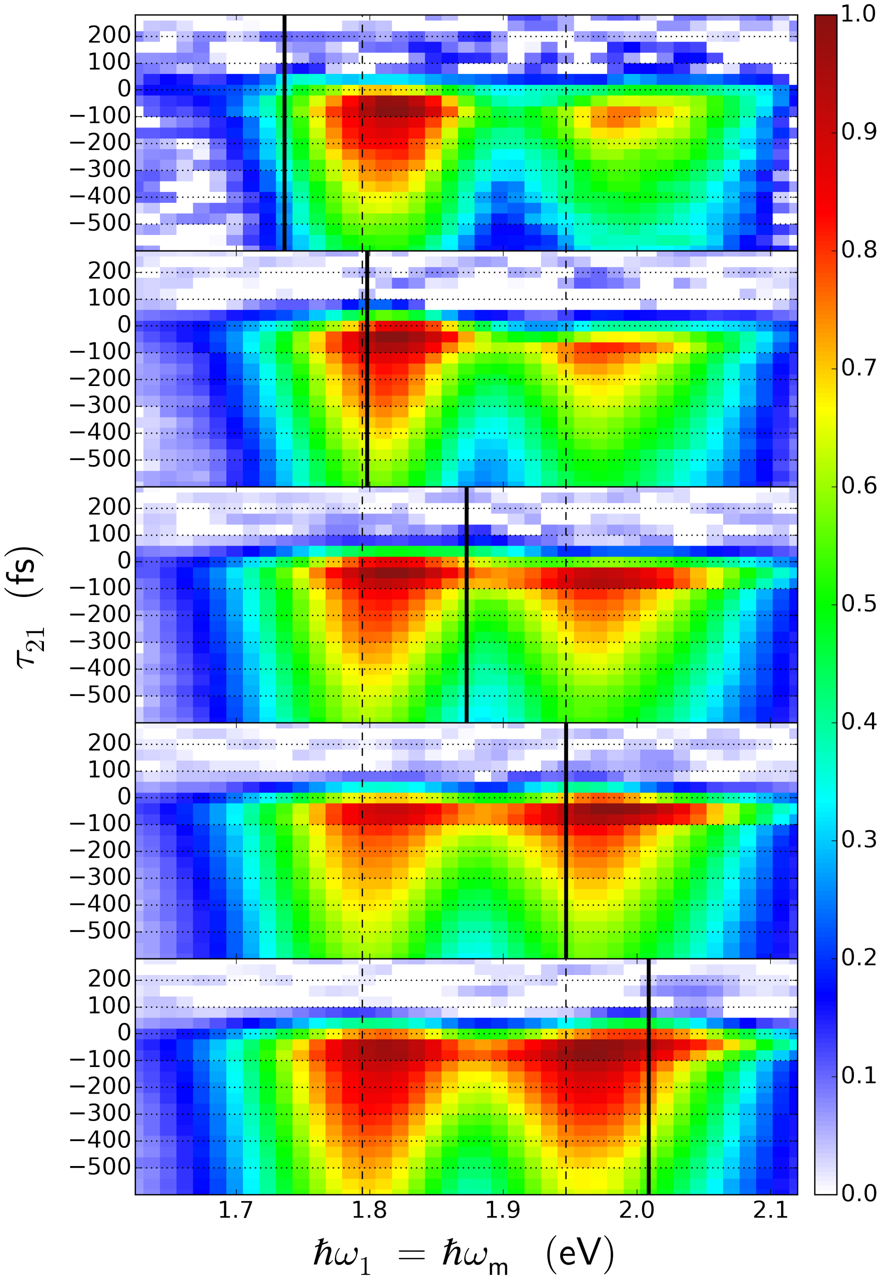

Figure 7.10: Mixed ω_1—τ_{21} time—frequency representations of the 3D data set at five ascending ω_2 excitation frequencies (solid black lines) showing the impact of the ω_2 excitation frequency on the ω_1 spectral line shape as a function of time. The A and B exciton energies are marked as dashed lines within each spectrum.

Each subplot in Figure 7.10 is similar to published pump-probe, transient absorption, multidimensionaland transient reflection experiments that have measured the electronc dynamics of the A and B excitons.

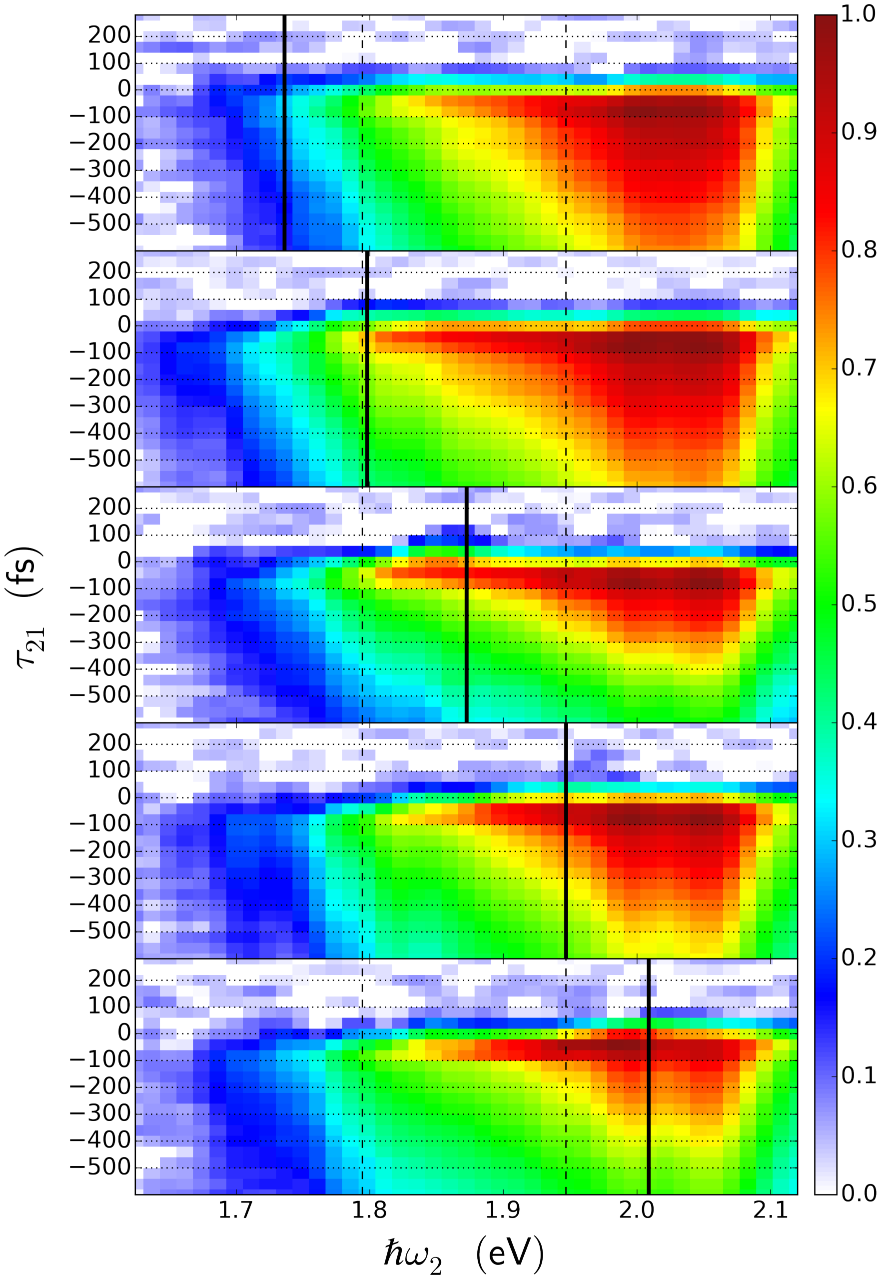

Figure 7.11: Mixed ω_2—τ_{21} time—frequency representations of the 3D data set at five ascending ω_1 probe frequencies (solid black lines) showing the impact of the ω_1 excitation frequency on the ω_2 spectral line shape as a function of time. The A and B exciton energies are marked as dashed lines within each spectrum.

[20, 21, 4, 22, 23, 24, 26, 45] These previous experiments measure relaxation dynamics on the same ≈400-600 fs time scale that is characteristic of Figure 7.10.

Our experiments also show how the spectral features change as a function of the ω_2 excitation frequency. The top to subplots of Figure 7.10 reflect the changes in the AA and BA features, while the bottom two subplots reflect the changes in the AB and BB features. The figure highlights the changes in the relative amplitude of the A and B features as a function of excitation frequency. Both the line shapes and the dynamics of the spectral features are very similar. Figure 7.11 is an excitation spectrum that shows that the dynamics of the spectral features do not depend strongly on the ω_1 frequency.

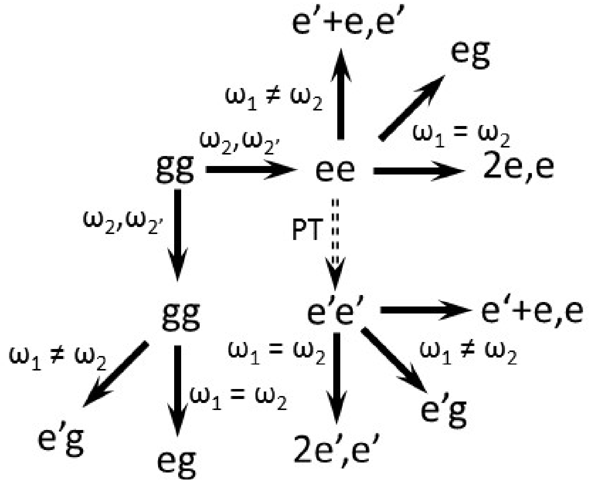

Figure 7.12: Liouville pathways for Figure 7.10. gg and ee designate ground- and excited-state populations, the eg, 2e,e, and e′+e,e represent the excitonic and biexcitonic output coherences, and the arrows are labeled with the frequencies or population transfer responsible for the transitions. e and e′ represent either A or B excitonic states.

The spectral features in Figures 7.9, 7.10 and 7.11 depend on the quantum mechanical interference effects caused by the different pathways. Figure 7.12 shows all of the Liouville pathways required to understand the spectral features. [46, 47] These pathways correspond to the time orderings labeled V and VI in Figure 7.7b. The letters denote the density matrix elements, ρ_{ij}, where g representest the ground state and e, e′ represent any excitonic state. Interaction with the temporally overlapped ω_2 and $\omega_{2'}$ pulses excites the ee excited-state population and bleaches the ground-state population. Subsequent interaction with ω_1 creates the output coherences for the diagonal spectral features when $\omega_1 = \omega_2$ or the cross-peak features when $\omega_1 \neq \omega_2$. The stimulated emission (SE) and ground-state bleaching (GSB) pathways create the eg or e′g output coherences from the ee and gg populations, respectively, while the excited-state absorption pathway creates the 2e,e or e′+e,e biexcitonic output coherences. Figure 7.12 also includes a population transfer pathway from the ee excited-state population to an e′e′ population from which similar SE and ESA pathways occur. Since the ESA pathways destructively interfere with the SE and GSB pathways, the output singal depends on the differences between the pathways. Factors that change the biexcitonic output coherences such as the transition moments, state filling (Pauli blocking), frequency shifts, or dephasing rate changes will control the output signal. State filling and ground-state depletion are important factors for MoS_2 since the transitions excite specific electron and hole spin and valley states in individual layers.

The state-filling and ground-state bleaching effects on the diagonal and cross-peak features in Figure 7.9 depend on the spin and valley states in the output coherence. [19] The effects of these spins will disappear as the spin and valley states return to equilibrium. [48, 49, 50] If we assume spin relaxation is negligible, the FWM transitions that create the diagonal features involve either the A or B ESA transitions, so the resulting 2e,e state includes two spin-aligned conduction band electrons and valence band holes. Similarly, the cross-peak regions denoted by AB or BA in Figure 7.1d will have two transitions involving an A exciton, so the initial e'+e,e state will include antialigned spins. A quantitative treatment of the cancellation effects between the GSB, SE, and ESA pathways requries knowledge of the transition moments and state degeneracies and is beyond the scope of this paper. [51]

The most important characteristic of the experimental spectra is the contrast between the absence of well-resolved excitonic features that depend on ω_2 in Figures 7.9 and 7.11 and the well-defined excitonic features that depend on ω_1. It is also important to note that the projections of the signal amplitude onto the ω_2 axis in Figure 7.9 match closely with the continuum features in the absorption spectrum and that the line shapes of the features along the ω_2 axis in Figure 7.11 do not change appreciably for different delay times or ω_1 values. It shoudl be noted that the excitation pulse bandwidth (see Figure 7.7e) contributes to the absence of well-resolved A and B excitonic features along ω_2. The similarity to the continuum states in the absorption spectrum and the absence of a strong dependence on ω_1 show that the continuum states observed at higher ω_2 frequencies participate directly in creating the final output coherences and that their increasing importance reflects the increasing absorption strength of higher energy continuum states. In contrast, the features dependent on ω_1 in Figures 7.9 and 7.10 match the line shapes of the A and B excitonic resonances. Although the relative amplitudes of the spectral features depend on the ω_2 frequency, they do not depend strongly on the delay times. These characteristics show that hot A and B excitonic states undergo rapid intraband population relaxation over a <70 fs time scale set by excitation pulses to the A and B excitonic states excited by ω_1.

A central feature of Figures 7.9 and 7.10 is that the AB region is much brighter than the BA region. This difference is suprising because simple models predict cross-peaks of equal amplitude, as depicted in Figure 7.1d. The symmetry in simple models arises because the AB and BA cross-peaks involve the same four transitions. The symmetry between AB and BA may be broken by material processes such as population relaxation and transfer, the output coherence dephasing rates, and the bleaching and state-filling effects of the valence and conduction band states involved in the transitions.

We believe that ultrafast intraband population transfer breaks the symmetry of AB and BA cross-peaks. For the BA peak, the interactions with ω_2 and $\omega_{2'}$ generate only A excitons that do not relax on <70 fs time scales. For the AB peak, ω_2 and $\omega_{2'}$ generate two kinds of excitons: (1) B excitons and (2) hot excitons in the A band. Relaxation to A may occur by interband transitions of B excitons or intraband transitions of hot A excitons. Either will lead to the GSB, SE, and ESA shown in the ee $\rightarrow$ e$'$e$'$ population transfer pathways of Figure 7.12. This relaxation must occur on the time scale of our pulse-width since the cross-peak asymmetry is observed even during temporal overlap. We believe that intraband relaxation of hot A excitons is the main factor in breaking the symmetry between AB and BA cross-peaks. Figure 7.10 shows that B $\rightarrow$ A interband relaxation occurs on a longer time scale. The B/A ratio is higher when ω_2 is resonant with the B excitonic transition than when ω_2 is lower than the A exciton frequency (the top subplot). If population transfer of holes from the B to A valence bands occurred during temporal overlap, the B/A ratio would be independent of pump frequency at $\tau_2 1 < 0$.

Figure 7.13 shows the delay transients at the different frequencies shown in the 2D spectrum. The colors of the dots on the 2D frequency-frequency spectrum match the colors of the transients. The transients were taken with a smaller step size and a longer time scale than the delay space explored in the 3D data set. The transients are quite similar. Our data are consistent with both monomolecular biexponential and bimolecular kinetic models and cannot discriminate between them. We have fit the decay kinetics to a single exponential model with a time constant of 680 fs and an offset that represents the long time decay. The 680 fs decay is similar to previously published pump-probe and transient absorption experiments. [22, 23, 52]

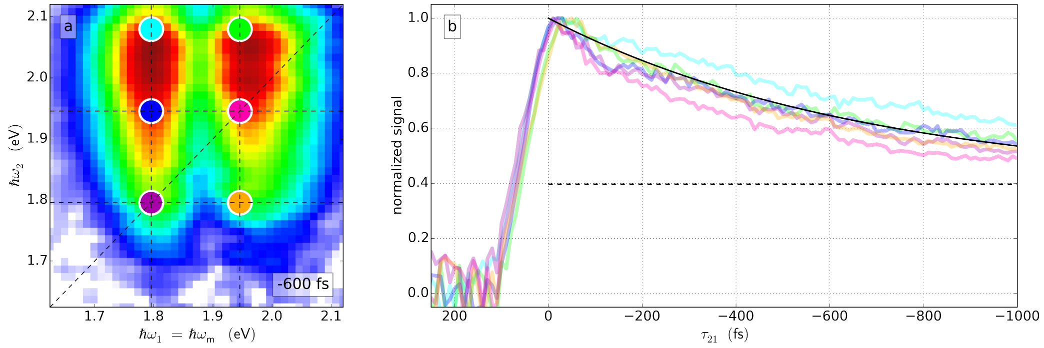

Figure 7.13: Transients taken at the different ω_1 and ω_2 frequencies indicated by the colored markers on the 2D spectrum. The dynamics are assigned to a 680 fs fast time constant (black solid line) and a slow time constant represented as an unchanging offset over this timescale (black dashed line).

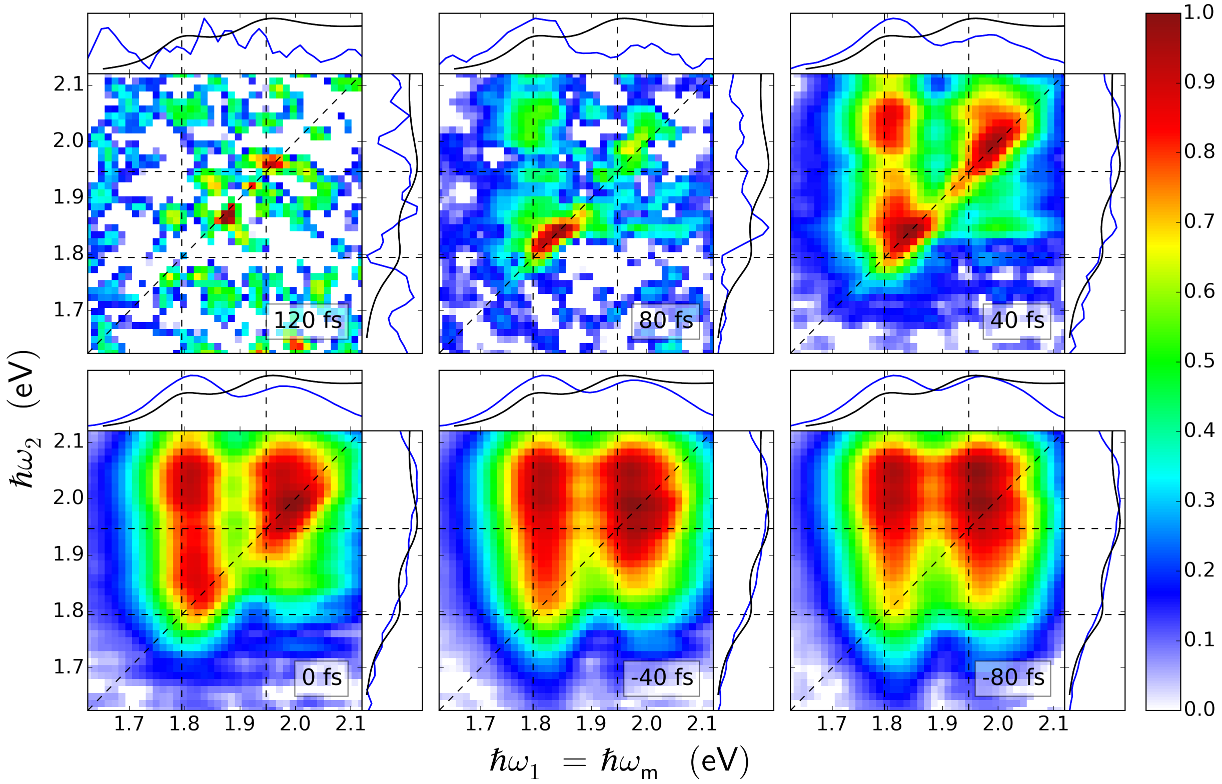

Figure 7.14: 2D frequency-frquency spectra near zero τ_{21} delay times. The signal amplitude is normalized to the brightest features in each spectrum.

The spectral features change quantitatively for delay times near temporal overlap. Figure 7.14 shows a series of 2D spectra for both positive and negative τ_{21} delay times with $\tau_{22'} = 0$. Each spectrum is normalized to its brightest feature. The spectra at positive τ_{21} delay times become rapidly weaker as the delay times become more positive until the features vanish into the noise at +120 fs. The spectra also develop more diagonal character as the delay time moves from negative to positive values. The AB cross-peak is also a strong feature in the spectrum at early times.

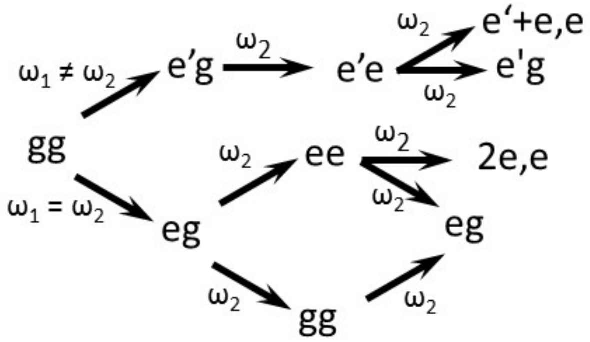

Figure 7.15: Liouville pathways for the ω_1, ω_2, and $\omega_{2'}$ time ordering of pulse interactions. e and e′ represent either A or B excitonic states.

The pulse overlap region is complicated by the multiple Liouville pathways that must be considered. Additionally, interference between scattered light from the ω_1 excitation beam and the output signal becomes a larger factor as the FWM signal decreases. Figure 7.15 shows the ω_1, ω_2, and $\omega_{2'}$ time ordered pathway that becomes and important consideration for positive τ_{21} delay times. Since $\tau_{22'} = 0$, the initial ω_1 pulse creates an excited-state coherence, while the subsequent ω_2 and $\omega_{2'}$ pulses create the output coherence. The output signal is only important at short $\tau_{21} > 0$ values because the initially excited coherence dephases very rapidly. When $\omega_1 \neq \omega_2$, the first two interactions create an e′e zero quantum coherence that also dephases rapidly. However, when $\omega_1 = \omega_2$, the first two interactions create an ee, gg population difference that relaxes on linger time scales. The resulting signal will therefore appear as the diagonal feature in Figure 7.14 (*e.g.*, see the +40 fs 2D spectrum). In addition to the diagonal feature in Figure 7.14, there is also a vertical feature when ω_1 is resonant with the A excitonic transition as well as the AB cross-peak. These features are attributed to the pathways in Figure 7.12. Although these pathways are depressed when $\tau_{21} > 0$, there is sufficient temporal overlap between the ω_2, $\omega_{2'}$, and ω_1 pulses to make their contribution comparable to those in Figure 7.15. More positie values of τ_{21} emphasize the Figure 7.15 pathways over the Figure 7.12 pathways, accounting for the increasing percentage of diagonal character at increasingly positive delays.

7.4 Conclusions

This paper presents the first coherent multidimensional spectroscopy of MoS_2 thin films. CMDS methods are related to the earlier ultrafast pump-probe and transient absorption methods since they all share bleaching, stimulated emission, Pauli blocking, and excited-state absorption pathways, but they differ in how these pathways define the spectra. In addition, CMDS methods have many additional pathways that become important when the coherence dephasing times are longer than the excitation pulse widths. In this work, the dephasing times are short so the pathways are identical to transient absorption. This work reports the first frequency-frequency-delay spectra of MX_2 samples. These spectra are complementary to previous work because they allow a direct comparison between the initially excited excitonic states and the states creating the final output coherence. The spectra show that the same hot A and B exciton continuum states that are observed in the absorption spectrum also dominate the CMDS excitation spectra. They also show that rapid, ¡70 fs intraband relaxation occurs to create the band-edge A and B excitonic features observed in the CMSD spectrum. The relative intensity of the diagonal peak features depends on the relative absorption strength of the A and B excitons. The relative intensity of cross-peak features in the 2D spectra depends on the excitation frequency. Excitation at or above the B exciton feature creates strong cross-peaks associated with hot A and B excitons that undergo ultrafast intraband population transfer. Excitation below the B excitonic feature creates a weak cross-peak indicating A-induced B-state bleaching but at a lower signal level corresponding to the lower optical density at this energy. Population relaxation occurs over $\approx$680 fs, either by transfer to traps or by bimolecular charge recombination.

These experiments provide the understanding of MoS_2 coherent multidimensional spectra that will form the foundation required to measure the dynamical processes occurring in more complex MoS_2 and other TMDC heterostructures with quantum-state resolution. The frequency domain based multiresonant CMDS methods described in this paper will play a central role in these measurements. They use longer, independently tunable pulses that provide state-selective excitation over a wide spectral range without the requirement for interferometric stability.

Chapter 8

PEDOT:PSS

Chapter 9

Pyrite

Chapter 10

BiVO4

pass

Part IV

Appendix

Appendix A

Public

A.1 Chemical systems

Chemical systems are complex! They contain many molecules (10^{25} in a cup of coffee, 1 trillion in each human cell). These molecules have multiple interaction modes, both internal (intramolecular) and external (intermolecular). The reactivity of the system taken as a whole can be dominated by very rare but very important species, *e.g.* catalysts.

Despite this complexity, scientists have gotten very good at describing chemical systems through representations of dynamic equilibrium. In such situations, several key parameters emerge:

- concentration
- timescale (rate)
- lengthscale

A.1.1 Concentration

A.1.2 Timescale

A.1.3 Lengthscale

A.2 Analytical chemistry

Traditionally, chemists have seen fit to divide themselves into four specializations: analytical, inorganic, organic, and physical. In recent years, materials chemistry and chemical biology have become specializations in their own right. This dissertation focuses on analytical chemistry.

Analytical chemists separate, identify, and quantify chemical systems. To do this, we build instruments that exploit physical properties of the chemical components:

- separation science (chromatography, electrophoresis)
- mass spectrometry
- electrochemistry
- microscopy
- spectroscopy

Spectroscopy is a family of strategies that exploit the interaction of chemical systems with light.

A.3 Spectroscopy

Molecules respond to electric fields. Static electric fields cause charged molecules (ions) to move, as in electrophoresis and mass spectrometry. Oscillating electric fields, also known as light, can interact directly with the molecules themselves, driving transitions. However, these transitions can only be driven with the appropriate frequency of light (resonance). Different frequencies (colors) of light interact with different kinds of transitions, revealing different features of the molecule of interest.

A.3.1 Nonlinear spectroscopy

Spectroscopy is fantastic, but sometimes simple experiments don't reveal everything. Nonlinear spectroscopy uses multiple electric fields simultaniously, revealing even more information about the chemical system.

A.4 Instrumentation

To accomplish nonlinear spectroscopy, specialized light sources are needed:

- gigantic electric fields
- ultrafast time resoution
- tunable frequencies

A.4.1 LASER

These sources are made using Light Amplified by the Stimulated Emission of Radiation (LASER).

By keeping a wide range ofr colors in phase simulatniously, we are able to create truly ultrafast pulses of light. The work presented in this dissertation was primarily taken using a 35 fs 1 KHz system.

35 fs (35×10^{15} second) pulses are incredibly short:

$$\frac{\text{pulse duration (35 fs)}}{\text{time between pulses (1 ms)}} \approx \frac{\text{5.75 months}}{\text{age of universe (13.7 billion years)}} \tag{A.1}$$

proportionally, our sample spends 6 months in the "sun" for every age of the unverse in the dark.

Because all of the energy within the pulse is compressed to such a short period of time, these pulses are also incredibly powerful:

$$\frac{\text{energy per pulse (4 mJ)}}{\text{pulse duration (35 fs)}} \approx \frac{\text{US electricity generation}(5.43 \times 10^{11}\, W)}{5} \tag{A.2}$$

this laser outputs electric fields one fifth as powerful as total US electricity generation (2016).

A.4.2 OPA

Appendix B

Procedures

Appendix C

Hardware

In this chapter I collect some of the specific hardware contribution details that do not belong in the body of the dissertation.

C.1 Adjustable periscopes

OPAs output horizontal or vertical polarizations according to which tuning process is used. Our experiments are opinionated about polarization, so some strategy for aligning polarization is necessary. In addition, it is useful to bring all excitation beams to the same height. To this end, I designed and constructed two adjustable periscopes. Each periscope is designed to bring OPA output to table height standard (5 inches) while either keeping or switching polarization. Both polarization configurations take the same path length, so source polarization can be switched without large changes to zero delay. All of this is done with just two (switched polarization) or three (kept polarzation) reflections. A picture of these periscopes is shown in C.1.

While these periscopes are easy to align, their unique design means that it is not necessarily obvious what the correct strategy is. The following strategy will always converge:

1. use two “magic” apertures along the output beamline

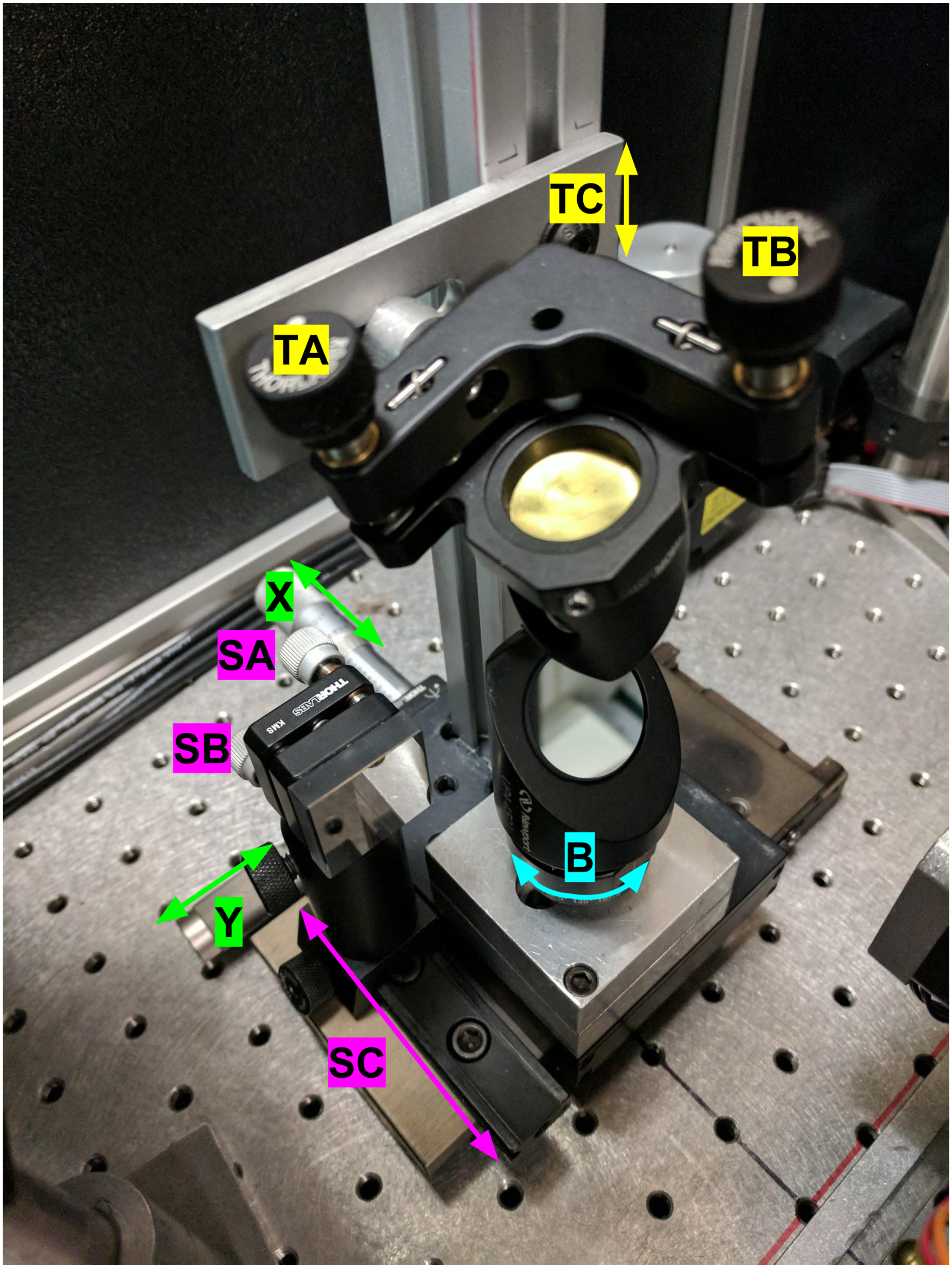

Figure C.1: CAPTION TODO

2. in flipped polarization (two mirror configuration):
    - use the stage (green X, Y) to align near aperture
    - use the upper mirror (yellow TA, TB) to align far aperture
    - iterate above
3. in kept polarization (three mirror configuration):
    - use stage X (green X) and upper mirror height (yellow TC) to align near aperture
    - use lower mirror (pink SA, SB) to align far aperture
    - iterate above

The kept polarization alignment is derivative of the fixed polarization alignment. One must ensure that the fixed polarization is correctly aligned at all times.

Mirror B (aqua) is magnetically mounted to switch between polarization conditions. Ensure that the lower turning mirror (pink) does not bump into mirror B (aqua) in polarization swtiching configuration. The lower turning mirror is on a rail (pink SC). This rail is a rough adjust for the same degree of freedom as pink SA. Adjust the rail only to ensure that the beam is roughly centered on the free aperture of the turning mirror.

The first reflection is often accomplished using a wedge, as OPA output may be strong enough to damage downstream optics. This optic can and should be replaced if more of the OPA output is desired on the table (keeping damage thresholds in mind).

C.1.1 Wedge polarization preference

TODO: wedges will be more efficent at reflecting horizontal / vertical at 45 degrees

C.2 Automated transmissive filters

TODO

C.3 Electronics

TODO

Appendix D

Errata

In this appendix I list the errors I am currently aware of in my publications and associated work.

D.1 Czech 2015

The following is an errata for Czech et al. [53], published in November 2015.

- Reference 13 is identical to reference 9.
- In the last paragraph of the introduction the sentence “The experimental spectra differ from the simple 2D spectrum shown in Figure 1d and those of earlier CMDS experiments with model systems” appears. This sentence cites references 6 through 10. Instead, it should cite references 15 through 20.
- In the last paragraph begining on page 12148, the text “Automated delay stages and neutral density filters set the excitation time delays over all values of τ_{21} with $\tau_{22} = 0$” appears. For the second τ, the subscript should read $22'$, not 22.
- Caption of Figure 5 reads, in part: "showing the impact of the ω_1 excitation frequency on the ω_1 spectral line shape". This should instead read "showing the impact of the ω_1 excitation frequency on the ω_2 spectral line shape". The subscript on the last ω should be a 2 and not a 1.

- Figure 6 e'+e,e' should read e'+e,e and vice versa.

Appendix E

Colophon

This chapter lays out the technical aspects of this dissertation as a software and data product, including instructions for obtaining the source and regeneration of figures and documents.

Bibliography

[1] Daniel Kahneman. *Thinking, Fast and Slow*. Farrar, Straus and Giroux, 2013. ISBN: 9780374533557.

[2] Duckhwan Lee and Andreas C. Albrecht. “A Unified View of Raman, Resonance Raman, and Fluorescence Spectroscopy (and their Analogues in Two-Photon Absorption”. In: *Advances in infrared and Raman Spectroscopy*. Ed. by R. J. H. Clark and R. E. Hester. 1st ed. London; New York, 1985. Chap. 4, pp. 179–213. ISBN: 9780471906742.

[3] Jacques Pankove. *Optical Processes in Semiconductors*. Dover Publications, 1975. ISBN: 9780486602752.

[4] Nardeep Kumar, Jiaqi He, Dawei He, Yongsheng Wang, and Hui Zhao. “Charge carrier dynamics in bulk MoS2 crystal studied by transient absorption microscopy”. In: *Journal of Applied Physics* 113.13 (2013), p. 133702. DOI: 10.1063/1.4799110.

[5] Ji-xin Cheng, Andreas Volkmer, Lewis D Book, and X Sunney Xie. “An Epi-Detected Coherent Anti-Stokes Raman Scattering (E-CARS) Microscope with High Spectral Resolution and High Sensitivity”. In: *The Journal of Physical Chemistry B* 105.7 (Feb. 2001), pp. 1277–1280. DOI: 10.1021/jp003774a.

[6] Austin P. Spencer, Hebin Li, Steven T. Cundiff, and David M. Jonas. “Pulse Propagation Effects in Optical 2D Fourier-Transform Spectroscopy: Theory”. In: *The Journal of Physical Chemistry A* 119.17 (2015), pp. 3936–3960. DOI: 10.1021/acs.jpca.5b00001.

[7] Jo Erskine Hannay, Carolyn MacLeod, Janice Singer, Hans Petter Langtangen, Dietmar Pfahl, and Greg Wilson. “How do scientists develop and use scientific software?” In: *2009 ICSE Workshop on Software Engineering for Computational Science and Engineering*. Institute of Electrical and Electronics Engineers (IEEE), May 2009. DOI: 10.1109/secse.2009.5069155.

[8] Judith Segal. “When Software Engineers Met Research Scientists: A Case Study”. In: *Empirical Software Engineering* 10.4 (Oct. 2005), pp. 517–536. DOI: 10.1007/s10664-005-3865-y.

[9] Tobias Brixner, Tomas Mancal, Igor V. Stiopkin, and Graham R. Fleming. “Phase-stabilized two-dimensional electronic spectroscopy”. In: *The Journal of Chemical Physics* 121.9 (2004), p. 4221. DOI: 10.1063/1.1776112.

[10] Lena A Yurs, Stephen B. Block, Andrei V Pakoulev, Rachel S. Selinsky, Song Jin, and John Wright. “Multiresonant Coherent Multidimensional Electronic Spectroscopy of Colloidal PbSe Quantum Dots”. In: *The Journal of Physical Chemistry C* 115.46 (Nov. 2011), pp. 22833–22844. DOI: 10.1021/jp207273x.

[11] Koichi Furuta, Masanori Fuyuki, and Akihide Wada. “Cross-Term Selective, Two-Pulse Correlation Measurements by Phase-Shifted Parallel Modulation for Analysis of a Multi-Photon Process”. In: *Applied Spectroscopy* 66.12 (Dec. 2012), pp. 1475–1479. DOI: 10.1366/12-06657.

[12] Ramūnas Augulis and Donatas Zigmantas. "Two-dimensional electronic spectroscopy with double modulation lock-in detection: enhancement of sensitivity and noise resistance." In: *Optics express* 19.14 (June 2011), pp. 13126–13133. DOI: `10.1364/OE.19.013126`.

[13] Ismael A. Heisler, Roberta Moca, Franco V A Camargo, and Stephen R. Meech. "Two-dimensional electronic spectroscopy based on conventional optics and fast dual chopper data acquisition". In: *Review of Scientific Instruments* 85.6 (June 2014), p. 063103. DOI: `10.1063/1.4879822`.

[14] Ivan C. Spector, Courtney M. Olson, Christopher J. Huber, and Aaron M. Massari. "Simple fully reflective method of scatter reduction in 2D-IR spectroscopy". In: *Optics Letters* 40.8 (Apr. 2015), pp. 1850–1852. DOI: `10.1364/OL.40.001850`.

[15] Brian L. McClain, Ilya J. Finkelstein, and M. D. Fayer. "Vibrational echo experiments on red blood cells: Comparison of the dynamics of cytoplasmic and aqueous hemoglobin". In: *Chemical Physics Letters* 392.4-6 (July 2004), pp. 324–329. DOI: `10.1016/j.cplett.2004.05.080`.

[16] Qing Hua Wang, Kourosh Kalantar-Zadeh, Andras Kis, Jonathan N. Coleman, and Michael S. Strano. "Electronics and optoelectronics of two-dimensional transition metal dichalcogenides". In: *Nature Nanotechnology* 7.11 (Nov. 2012), pp. 699–712. DOI: `10.1038/nnano.2012.193`. URL: `https://doi.org/10.1038/nnano.2012.193`.

[17] Kin Fai Mak, Changgu Lee, James Hone, Jie Shan, and Tony F. Heinz. "Atomically ThinMoS2: A New Direct-Gap Semiconductor". In: *Physical Review Letters* 105.13 (Sept. 2010). DOI: `10.1103/physrevlett.105.136805`.

[18] Alejandro Molina-Sánchez, Davide Sangalli, Kerstin Hummer, Andrea Marini, and Ludger Wirtz. "Effect of spin-orbit interaction on the optical spectra of single-layer, double-layer, and bulk MoS2". In: *Physical Review B* 88.4 (July 2013). DOI: `10.1103/physrevb.88.045412`.

[19] Xiaodong Xu, Wang Yao, Di Xiao, and Tony F. Heinz. "Spin and pseudospins in layered transition metal dichalcogenides". In: *Nature Physics* 10.5 (Apr. 2014), pp. 343–350. DOI: `10.1038/nphys2942`.

[20] Di Xiao, Gui-Bin Liu, Wanxiang Feng, Xiaodong Xu, and Wang Yao. "Coupled Spin and Valley Physics in Monolayers ofMoS2and Other Group-VI Dichalcogenides". In: *Physical Review Letters* 108.19 (May 2012). DOI: `10.1103/physrevlett.108.196802`.

[21] H. Fang, C. Battaglia, C. Carraro, S. Nemsak, B. Ozdol, J. S. Kang, H. A. Bechtel, S. B. Desai, F. Kronast, A. A. Unal, G. Conti, C. Conlon, G. K. Palsson, M. C. Martin, A. M. Minor, C. S. Fadley, E. Yablonovitch, R. Maboudian, and A. Javey. "Strong interlayer coupling in van der Waals heterostructures built from single-layer chalcogenides". In: *Proceedings of the National Academy of Sciences* 111.17 (Apr. 2014), pp. 6198–6202. DOI: `10.1073/pnas.1405435111`.

[22] Zhaogang Nie, Run Long, Linfeng Sun, Chung-Che Huang, Jun Zhang, Qihua Xiong, Daniel W. Hewak, Zexiang Shen, Oleg V. Prezhdo, and Zhi-Heng Loh. "Ultrafast Carrier Thermalization and Cooling Dynamics in Few-Layer MoS2". In: *ACS Nano* 8.10 (Oct. 2014), pp. 10931–10940. DOI: `10.1021/nn504760x`.

[23] Dezheng Sun, Yi Rao, Georg A. Reider, Gugang Chen, Yumeng You, Louis Brézin, Avetik R. Harutyunyan, and Tony F. Heinz. "Observation of Rapid Exciton–Exciton Annihilation in Monolayer Molybdenum Disulfide". In: *Nano Letters* 14.10 (Oct. 2014), pp. 5625–5629. DOI: `10.1021/nl5021975`.

[24] Sangwan Sim, Jusang Park, Jeong-Gyu Song, Chihun In, Yun-Shik Lee, Hyungjun Kim, and Hyunyong Choi. "Exciton dynamics in atomically thin MoS2: Interexcitonic interaction and broadening kinetics". In: *Physical Review B* 88.7 (Aug. 2013). DOI: `10.1103/physrevb.88.075434`.

[25] Patanjali Kambhampati. “Unraveling the Structure and Dynamics of Excitons in Semiconductor Quantum Dots”. In: *Accounts of Chemical Research* 44.1 (Jan. 2011), pp. 1–13. DOI: 10.1021/ar1000428.

[26] Kin Fai Mak, Keliang He, Jie Shan, and Tony F. Heinz. “Control of valley polarization in monolayer MoS2 by optical helicity”. In: *Nature Nanotechnology* 7.8 (June 2012), pp. 494–498. DOI: 10.1038/nnano.2012.96.

[27] Steven T. Cundiff. “Coherent spectroscopy of semiconductors”. In: *Optics Express* 16.7 (Mar. 2008), p. 4639. DOI: 10.1364/oe.16.004639.

[28] Daniel B. Turner, Katherine W. Stone, Kenan Gundogdu, and Keith A. Nelson. “Three-dimensional electronic spectroscopy of excitons in GaAs quantum wells”. In: *The Journal of Chemical Physics* 131.14 (Oct. 2009), p. 144510. DOI: 10.1063/1.3245964.

[29] Daniel D. Kohler, Stephen B. Block, Schuyler Kain, Andrei V. Pakoulev, and John C. Wright. “Ultrafast Dynamics within the 1S Exciton Band of Colloidal PbSe Quantum Dots Using Multiresonant Coherent Multidimensional Spectroscopy”. In: *The Journal of Physical Chemistry C* 118.9 (Mar. 2014), pp. 5020–5031. DOI: 10.1021/jp412058u. URL: https://doi.org/10.1021/jp412058u.

[30] Graham B. Griffin, Sandrine Ithurria, Dmitriy S. Dolzhnikov, Alexander Linkin, Dmitri V. Talapin, and Gregory S. Engel. “Two-dimensional electronic spectroscopy of CdSe nanoparticles at very low pulse power”. In: *The Journal of Chemical Physics* 138.1 (Jan. 2013), p. 014705. DOI: 10.1063/1.4772465. URL: https://doi.org/10.1063/1.4772465.

[31] Elad Harel, Sara M. Rupich, Richard D. Schaller, Dmitri V. Talapin, and Gregory S. Engel. “Measurement of electronic splitting in PbS quantum dots by two-dimensional nonlinear spectroscopy”. In: *Physical Review B* 86.7 (Aug. 2012). DOI: 10.1103/physrevb.86.075412. URL: https://doi.org/10.1103/physrevb.86.075412.

[32] S. T. Cundiff, M. Koch, W. H. Knox, J. Shah, and W. Stolz. “Optical Coherence in Semiconductors: Strong Emission Mediated by Nondegenerate Interactions”. In: *Physical Review Letters* 77.6 (Aug. 1996), pp. 1107–1110. DOI: 10.1103/physrevlett.77.1107. URL: https://doi.org/10.1103/physrevlett.77.1107.

[33] D. Birkedal, V. G. Lyssenko, J. M. Hvam, and K. El Sayed. “Continuum contribution to excitonic four-wave mixing due to interaction-induced nonlinearities”. In: *Physical Review B* 54.20 (Nov. 1996), R14250–R14253. DOI: 10.1103/physrevb.54.r14250. URL: https://doi.org/10.1103/physrevb.54.r14250.

[34] M. U. Wehner, D. Steinbach, and M. Wegener. “Ultrafast coherent transients due to exciton-continuum scattering in bulk GaAs”. In: *Physical Review B* 54.8 (Aug. 1996), R5211–R5214. DOI: 10.1103/physrevb.54.r5211. URL: https://doi.org/10.1103/physrevb.54.r5211.

[35] Andrei V. Pakoulev, Mark A. Rickard, Kent A. Meyer, Kathryn Kornau, Nathan A. Mathew, David E. Thompson, and John C. Wright. “Mixed Frequency/Time Domain Optical Analogues of Heteronuclear Multidimensional NMR”. In: *The Journal of Physical Chemistry A* 110.10 (Mar. 2006), pp. 3352–3355. DOI: 10.1021/jp057339y. URL: https://doi.org/10.1021/jp057339y.

[36] Masihhur R. Laskar, Lu Ma, Santhakumar Kannappan, Pil Sung Park, Sriram Krishnamoorthy, Digbijoy N. Nath, Wu Lu, Yiying Wu, and Siddharth Rajan. “Large area single crystal (0001) oriented MoS2”. In: *Applied Physics Letters* 102.25 (June 2013), p. 252108. DOI: 10.1063/1.4811410. URL: https://doi.org/10.1063/1.4811410.

[37] A. Castellanos-Gomez, M. Barkelid, A. M. Goossens, V. E. Calado, H. S. J. van der Zant, and G. A. Steele. "Laser-Thinning of MoS2: On Demand Generation of a Single-Layer Semiconductor". In: *Nano Letters* 12.6 (June 2012), pp. 3187–3192. DOI: 10.1021/nl301164v. URL: https://doi.org/10.1021/nl301164v.

[38] Mariyappan Shanmugam, Chris A. Durcan, and Bin Yu. "Layered semiconductor molybdenum disulfide nanomembrane based Schottky-barrier solar cells". In: *Nanoscale* 4.23 (2012), p. 7399. DOI: 10.1039/c2nr32394j. URL: https://doi.org/10.1039/c2nr32394j.

[39] Andreas Volkmer, Ji-Xin Cheng, and X. Sunney Xie. "Vibrational Imaging with High Sensitivity via Epidetected Coherent Anti-Stokes Raman Scattering Microscopy". In: *Physical Review Letters* 87.2 (June 2001). DOI: 10.1103/physrevlett.87.023901. URL: https://doi.org/10.1103/physrevlett.87.023901.

[40] Fernando Perez and Brian E. Granger. "IPython: A System for Interactive Scientific Computing". In: *Computing in Science & Engineering* 9.3 (2007), pp. 21–29. DOI: 10.1109/mcse.2007.53. URL: https://doi.org/10.1109/mcse.2007.53.

[41] John D. Hunter. "Matplotlib: A 2D Graphics Environment". In: *Computing in Science & Engineering* 9.3 (2007), pp. 90–95. DOI: 10.1109/mcse.2007.55. URL: https://doi.org/10.1109/mcse.2007.55.

[42] Song-Lin Li, Hisao Miyazaki, Haisheng Song, Hiromi Kuramochi, Shu Nakaharai, and Kazuhito Tsukagoshi. "Quantitative Raman Spectrum and Reliable Thickness Identification for Atomic Layers on Insulating Substrates". In: *ACS Nano* 6.8 (Aug. 2012), pp. 7381–7388. DOI: 10.1021/nn3025173. URL: https://doi.org/10.1021/nn3025173.

[43] Mark A. Lukowski, Andrew S. Daniel, Fei Meng, Audrey Forticaux, Linsen Li, and Song Jin. "Enhanced Hydrogen Evolution Catalysis from Chemically Exfoliated Metallic MoS2 Nanosheets". In: *Journal of the American Chemical Society* 135.28 (July 2013), pp. 10274–10277. DOI: 10.1021/ja404523s. URL: https://doi.org/10.1021/ja404523s.

[44] Alan C. Eckbreth. "BOXCARS: Crossed-beam phase-matched CARS generation in gases". In: *Applied Physics Letters* 32.7 (Apr. 1978), pp. 421–423. DOI: 10.1063/1.90070.

[45] Markus Thomalla and Helmut Tributsch. "Photosensitization of Nanostructured TiO2 with WS2 Quantum Sheets". In: *The Journal of Physical Chemistry B* 110.24 (June 2006), pp. 12167–12171. DOI: 10.1021/jp061371q. URL: https://doi.org/10.1021/jp061371q.

[46] Andrei V. Pakoulev, Stephen B. Block, Lena A. Yurs, Nathan A. Mathew, Kathryn M. Kornau, and John C. Wright. "Multiply Resonant Coherent Multidimensional Spectroscopy: Implications for Materials Science". In: *The Journal of Physical Chemistry Letters* 1.5 (Mar. 2010), pp. 822–828. DOI: 10.1021/jz9003476. URL: https://doi.org/10.1021/jz9003476.

[47] Andrei V. Pakoulev, Mark A. Rickard, Kathryn M. Kornau, Nathan A. Mathew, Lena A. Yurs, Stephen B. Block, and John C. Wright. "Mixed Frequency-/Time-Domain Coherent Multidimensional Spectroscopy: Research Tool or Potential Analytical Method?" In: *Accounts of Chemical Research* 42.9 (Sept. 2009), pp. 1310–1321. DOI: 10.1021/ar900032g. URL: https://doi.org/10.1021/ar900032g.

[48] Hualing Zeng, Junfeng Dai, Wang Yao, Di Xiao, and Xiaodong Cui. "Valley polarization in MoS2 monolayers by optical pumping". In: *Nature Nanotechnology* 7.8 (June 2012), pp. 490–493. DOI: 10.1038/nnano.2012.95. URL: https://doi.org/10.1038/nnano.2012.95.

[49] Bairen Zhu, Hualing Zeng, Junfeng Dai, and Xiaodong Cui. “The Study of Spin-Valley Coupling in Atomically Thin Group VI Transition Metal Dichalcogenides”. In: *Advanced Materials* 26.31 (Apr. 2014), pp. 5504–5507. DOI: `10.1002/adma.201305367`. URL: `https://doi.org/10.1002/adma.201305367`.

[50] Cong Mai, Andrew Barrette, Yifei Yu, Yuriy G. Semenov, Ki Wook Kim, Linyou Cao, and Kenan Gundogdu. “Many-Body Effects in Valleytronics: Direct Measurement of Valley Lifetimes in Single-Layer MoS2”. In: *Nano Letters* 14.1 (Dec. 2013), pp. 202–206. DOI: `10.1021/nl403742j`. URL: `https://doi.org/10.1021/nl403742j`.

[51] Cathy Y. Wong and Gregory D. Scholes. “Using two-dimensional photon echo spectroscopy to probe the fine structure of the ground state biexciton of CdSe nanocrystals”. In: *Journal of Luminescence* 131.3 (Mar. 2011), pp. 366–374. DOI: `10.1016/j.jlumin.2010.09.015`. URL: `https://doi.org/10.1016/j.jlumin.2010.09.015`.

[52] Callum J. Docherty, Patrick Parkinson, Hannah J. Joyce, Ming-Hui Chiu, Chang-Hsiao Chen, Ming-Yang Lee, Lain-Jong Li, Laura M. Herz, and Michael B. Johnston. “Ultrafast Transient Terahertz Conductivity of Monolayer MoS2 and WSe2 Grown by Chemical Vapor Deposition”. In: *ACS Nano* 8.11 (Nov. 2014), pp. 11147–11153. DOI: `10.1021/nn5034746`. URL: `https://doi.org/10.1021/nn5034746`.

[53] Kyle J. Czech, Blaise J. Thompson, Schuyler Kain, Qi Ding, Melinda J. Shearer, Robert J. Hamers, Song Jin, and John C. Wright. “Measurement of Ultrafast Excitonic Dynamics of Few-Layer MoS2Using State-Selective Coherent Multidimensional Spectroscopy”. In: *ACS Nano* 9.12 (Dec. 2015), pp. 12146–12157. DOI: `10.1021/acsnano.5b05198`.